nature communications

Article

https://doi.org/10.1038/s41467-026-77196-7

The cortical microenvironment drives early immune organization and controls early osteoclastogenesis in bone healing

Received: 26 August 2025

Accepted: 18 August 2026

Published online: 27 August 2026

Check for updates

A list of authors and their affiliations appears at the end of the paper

Bone regeneration is a complex, tightly regulated process involving coordinated interactions of immune and stromal cells. Early phases of healing rely on the timely clearance of debris, a task primarily carried out by macrophages and osteoclasts. However, the sequence of events leading to the presence of osteoclasts at the fracture site and how this is shaped by local tissue microenvironments remains poorly understood, particularly at single-cell and spatial resolution. Using single-cell RNA sequencing and multi-epitope ligand cartography, we mapped the spatial organization of distinct cell compartments engaged in early fracture healing in both young and aged female mice at the start of healing. Surprisingly, we found that young mice exhibited an increased presence of activated osteoclasts at day 7, concentrated within the cortical niche. This compartment was also characterized by a spatially restricted immune response with a selective accumulation of distinct macrophage types jointly interacting with neutrophils and stromal cells. This raised the possibility that local cell organization influences osteoclast precursor differentiation. We identified a fracture-associated *Spp1*^{hi} macrophage subset enriched at the cortex, which represented a transitional monocyte-derived state that expressed early osteoclast differentiation transcripts and gave rise to osteoclasts ex vivo. Neutrophils preceded fracture-associated *Spp1*^{hi} macrophage accumulation and may promote their recruitment through chemotactic signaling. This coordination was less pronounced in aged mice despite preserved transcriptional states. In parallel, stromal cells in young animals displayed higher expression of essential niche factors, further supporting local osteoclastogenesis at the cortex. Together, our findings identify a distinct macrophage state that contains cells with osteoclast differentiation potential and reveal early, cortex-specific niche activity supporting osteoclastogenesis. This provides a new framework for understanding the initiation of spatial immune–stromal interactions for the early stages of regeneration.

Bone fractures are frequent and affect both young and aged patients. In almost all cases, fracture healing proceeds without complications to a scar-free regeneration[1–3]. Current treatments, including surgical stabilization and biological augmentation, generally support this natural healing process, yet delayed healing and non-unions still occur[4–6]. A better understanding of the cellular mechanisms that regulate bone regeneration is therefore still essential to improve therapeutic strategies.

e-mail: georg.duda@charite.de

Bone regeneration in long bones like the femur typically proceeds through secondary healing. Following fracture, the area is rapidly filled with a hematoma, initiating the inflammatory phase and creating a provisional matrix shaped by coagulation and platelet activation. During these early stages, the hematoma and adjacent bone compartments are infiltrated by immune cells[7,8], such as neutrophils[9,10] and macrophages[11,12], which orchestrate the transition from acute inflammation to tissue repair. Neutrophils appear rapidly and release chemotactic and proteolytic signals that condition the early microenvironment[9,13,14]. Macrophages soon follow and play multifaceted roles throughout the healing process.

Macrophages have historically been described along an M1/M2 axis, yet single-cell transcriptomics has revealed a far broader landscape of context-dependent phenotypes[11,12,15–17]. Among these, *Spp1*^{hi} macrophages represent a transcriptionally distinct and recurrently observed state across multiple tissues and inflammatory settings[16,18,19]. Within the bone environment, this functional diversity is further expanded by the presence of both monocyte-derived macrophages and long-lived tissue-resident populations such as osteal macrophages (osteomacs), which support osteoblast function and matrix homeostasis[20,21]. Their plasticity and responsiveness to local cues position macrophages as central regulators of the early fracture environment.

In addition to their regulatory roles, myeloid cells also give rise to osteoclasts, the multinucleated cells specialized in resorbing mineralized bones. Multiple myeloid subsets, including circulating *Ly6C*^{hi} monocytes[22], dendritic cell-like precursors[23], and tissue-resident macrophages[22], can differentiate into osteoclasts under stimulatory conditions. Much of this insight comes from in vitro differentiation systems in which myeloid cells are exposed to macrophage colony-stimulating factor (M-CSF; *Csf1*) and receptor activator of nuclear factor κB ligand (RANKL)[24,25], which have been instrumental for defining the molecular pathways of osteoclastogenesis.

However, the fracture microenvironment presents greater spatial and temporal complexity than these systems. Fracture healing occurs within spatially distinct niches, such as bone marrow and cortical bone, including the endosteum and periosteum, each characterized by unique cellular and signaling environments. Histological evidence further showed that osteoclasts appear at the endosteal and cortical surfaces much earlier than predicted by classical models of late-stage osteoclastogenesis[26–28]. Their rapid and spatially restricted emergence suggests that osteoclast differentiation is initiated rapidly during repair and is likely shaped by local tissue niches. Despite these insights, the mechanisms by which spatially distinct fracture microenvironments influence macrophage states and early osteoclast-associated differentiation programs in vivo remain poorly understood.

Aging adds a significantly higher layer of complexity to the bone microenvironment during fracture healing. Impaired healing in older individuals is associated with altered innate and adaptive immune responses[12] and, in parallel, increased osteoclast activity[29]. Yet, how aging affects fracture-associated macrophage and osteoclast differentiation trajectories remains unclear. Clarifying how niche context is coupled to distinct macrophage and osteoclast states in early phases of bone regeneration and how this is impacted by age is critical for understanding the very early immune regulation in bone healing.

In this study, we investigated the organization of immune-stromal interactions in time and space during bone healing at single-cell resolution. Using single-cell transcriptomics and multi-epitope ligand cartography (MELC), we identified a fracture-associated *Spp1*^{hi} macrophage subset enriched within the cortical microenvironment. They expressed higher levels of transcripts associated with early osteoclast differentiation and showed a higher capacity to differentiate to osteoclasts ex vivo, supporting that they contribute to osteoclast formation during bone healing. The accumulation of fracture-associated *Spp1*^{hi} macrophages was preceded by neutrophil infiltration and accompanied by increased expression of osteoclast-associated niche factors by cortical stromal cells, a response that was dampened in aged mice. These findings uncover spatially and temporally coordinated layering of fracture-associated macrophages and osteoclasts during bone regeneration and highlight the unique diversity of the cortical microenvironment during early bone regeneration.

Results

Osteoclast activity is delayed during early fracture healing of aged mice

To better understand how tissue microenvironments and aging influence macrophage and osteoclast differentiation during bone healing, we employed a standardized osteotomy model in young (12-week-old) and aged (52-week-old) mice, as previously published[7,11,30]. In short, a 0.7 mm osteotomy was introduced in the left femur and stabilized using a unilateral external fixator (MouseExFix, RISystem, Davos, Switzerland). This model allows us to examine the native influence of the tissue microenvironment on fracture healing and how this is altered with age, in the absence of any therapeutic intervention.

To determine whether osteoclasts are also active during the very early stages of bone healing, we focused on day 3 and day 7 post-osteotomy, preceding the classical remodeling phase typically assessed weeks after fracture[27]. Histological analysis of the fracture revealed the presence of bone fragments near the cortical edges at day 3, with partial clearance by day 7 (Supplementary Fig. 1A–D, Supplementary Data 1). To functionally evaluate osteoclast activity, we performed TRAP staining at both time points. In young mice, we observed a clear increase in TRAP-positive cells by day 7, particularly along the cortical bone surface and around residual bone debris (Fig. 1A, arrowheads), whereas this induction appeared less pronounced in aged animals (Fig. 1B). This early evidence of osteoclast activity in young mice indicates that osteoclast precursors are already present at the onset of healing, complementing other macrophage types that clear the hematoma and soft tissue remnants after fracture. Given the importance of removing necrotic or damaged tissues and even bone fragments as a prerequisite of any subsequent tissue regeneration[27], these findings suggest that early osteoclast activity and their differentiation from precursor cells recruited to the fracture site may be a critical process for an effective fracture repair process, and this process may be altered in aged mice.

Fracture-induced immune responses are highly compartmentalized

Given the enhanced osteoclast activity observed by day 7, we next sought to understand the cellular and molecular mechanisms underlying this early response. Since TRAP-positive cells were predominantly localized along the cortical bone surface, we hypothesized that distinct microenvironmental cues within the marrow and cortical compartments may differentially regulate osteoclast precursor differentiation.

To test this hypothesis, we employed single-cell RNA sequencing (scRNAseq) at different timepoints during fracture healing for young and aged mice to comprehensively profile all myeloid subsets and osteoclasts, as well as their local microenvironments within the marrow and cortical compartments during early fracture healing. To focus on the cell populations most relevant to bone regeneration, we analyzed cells that were recovered exclusively between the proximal and distal inner fixation pins. A two-step approach was used to separate the compartments (Fig. 2A). First, bone marrow-resident cells were collected through a direct flushing of the bone cavity. Then, cortex-adherent cells were liberated by subjecting the remaining cortical fragments to enzymatic digestion using a combination of collagenase and dispase. We analyzed cells from 30 mice present at day 3 and day 7 post-osteotomy, while intact marrow and cortex of age-matched mice served as controls. As an additional control, we also analyzed cells

https://doi.org/10.1038/s41467-026-77196-7

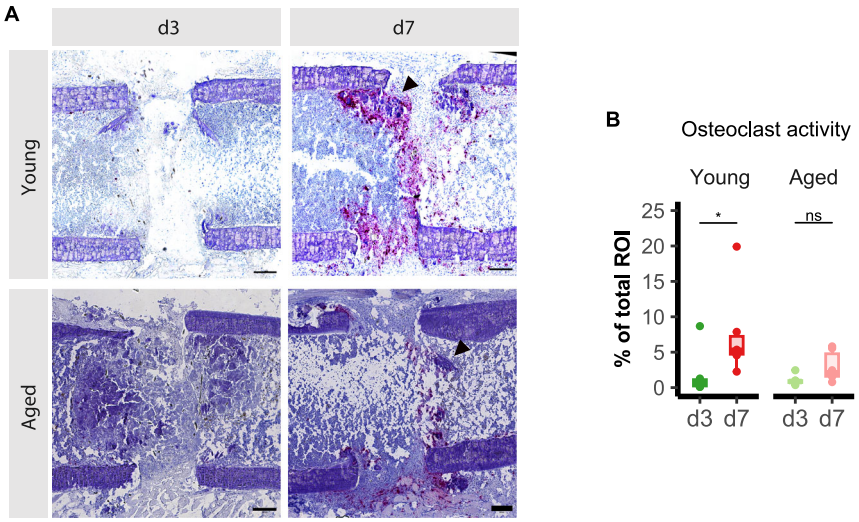

Fig. 1 | Early detection of osteoclast activity during fracture healing using TRAP staining. A Representative histological image showing TRAP (tartrate-resistant acid phosphatase) staining of the fracture gap at day 3 (d3) and day 7 (d7) post-osteotomy of young (12-week-old) and aged (52-week-old) animals. TRAP-positive osteoclasts (red) are primarily located along the cortical bone surface (purple), reflecting localized bone resorption activity in the early phase of healing. All femurs were oriented consistently, with the proximal end on the left and the distal end on the right side of each image. Scale bar = 200 μm. **B** Quantification of TRAP-positive area within the region of interest (ROI) (0.7 mm fracture gap, including 0.4 mm proximal and distal bone segments), performed using an in-house macro in Fiji. Box-and-whisker plots show the median (centre line), interquartile range (box limits), and whiskers extending to the most extreme values within 1.5× the inter-quartile range. Individual data points represent biological replicates (young d3, $n = 5$; young d7, $n = 6$; aged d3, $n = 5$; aged d7, $n = 5$). Age-dependent differences at each time point were evaluated using two-sided Wilcoxon rank-sum tests; Young: $P = 0.043$; ns = not significant. Source data are provided as a Source Data file.

obtained from the contralateral, uninjured femur. This approach, employed in prior studies of bone microenvironments[7,31], allowed us to create for the first time a single-cell atlas of both the marrow and cortex during the early onset of fracture healing.

In total, we recovered 178,416 cells across all conditions. To identify distinct cell populations among the compartments, we applied uniform manifold approximation and projection (UMAP) analysis for dimensionality reduction and Louvain clustering, which revealed 16 unique clusters (Fig. 2B–E). These clusters were annotated based on the expression of well-established marker genes, corresponding to a range of immune and stromal cell types, including 3 neutrophil clusters (Neutrophil-1, Neutrophil-2 and Neutrophil-3), hematopoietic stem cells (HSCs), eosinophil/basophil progenitors, erythrocytes, multipotent progenitors (MPPs), monocyte progenitors, monocytes, macrophages, dendritic cells, stromal cells, plasma cells and T and B cells (Fig. 2F). These annotations were validated by cross-referencing established markers from prior single-cell atlases of bone marrow and associated tissues, ensuring consistency with published datasets (Supplementary Fig. 1E, F, Supplementary Data 1)[31–34].

Following the identification of major cell populations across compartments, we next quantified the relative proportions of each cell type to systematically characterize how fracture injury reshapes the cellular landscape over time. In the marrow, progenitor populations seemed to have one of the most dynamics changes (Supplementary Fig. 2A). Neutrophil-1, likely resembling neutrophil progenitors (Supplementary Fig. 1), and monocyte progenitors expanded significantly (Benjamini-Hochberg-adjusted $p < 0.001$) at day 3. Notably, these expansions were not sustained as the progenitor levels returned to baseline level at day 7. In addition, mature immune cells also reacted to the osteotomy (Fig. 3A). For instance, macrophages showed an ~10-fold increase at day 3 followed by a similar decline at day 7, while dendritic cells and B cells showed the opposite (Supplementary Fig. 2A, Supplementary Data 2). These shifts are consistent with an emergency hematopoietic response to recruit innate effectors from the marrow at day 3, and afterwards an inflammatory resolution phase by day 7. At the cortex, the temporal analyses were characterized by an accumulation of innate immune cells (Fig. 3B). Macrophages also displayed here an ~30-fold increase on day 3 and a decline on day 7. Furthermore, the Neutrophil-3 cluster expanded almost 2-fold over time, reaching their peak at day 7. In contrast to the marrow, the cortex had more cell types, such as dendritic cells and B cells but also plasma cells and erythrocytes, declining in levels during our chosen timepoints (Supplementary Fig. 2B, Supplementary Data 2). This likely reflected not a loss of these cell types at the cortex, but rather a proportional shift for innate immunity at the cortex after osteotomy.

Having characterized the temporal immune and stromal dynamics within each individual compartment, we next compared the distribution of the populations between the marrow and cortex. Cell frequencies were comparable between compartments in intact femurs but changed significantly (Benjamini-Hochberg-adjusted $p < 0.05$) in a compartment-specific manner post-osteotomy (Fig. 3C). On day 3, the marrow displayed an enrichment in progenitors as well as B cells (Fig. 3D). In parallel, the cortex exhibited a relative enrichment of Neutrophil-3 cells and macrophages (Fig. 3D). By day 7, the distribution of cell populations was further altered between compartments. In the marrow, only Neutrophil-1 remained elevated while monocyte progenitors and B cells were no longer detected (Fig. 3E). At the cortex, macrophages and Neutrophil-3 continued to proportionally accumulate compared to their marrow counterparts (Fig. 3E). Additionally, stromal cells started to enrich at the cortex, despite limited changes in their overall abundance over time (Fig. 3A, B). These results indicated that osteotomy led to a selective recruitment of distinct cell types to the cortex and marrow in both young and aged animals.

Importantly, these injury-associated immune shifts in cell composition were not observed in contralateral bones (Supplementary Fig. 3, Supplementary Data 3). In contralateral bones, we did not detect a change in frequencies of any immune cell population, including neutrophils, macrophages, and stromal cells, and we detected no substantial difference in the frequency of these cell populations between the marrow and the cortex. These findings collectively highlight that fracture-induced immune responses are highly compartmentalized, governed by localized damage cues rather than systemic effects.

https://doi.org/10.1038/s41467-026-77196-7

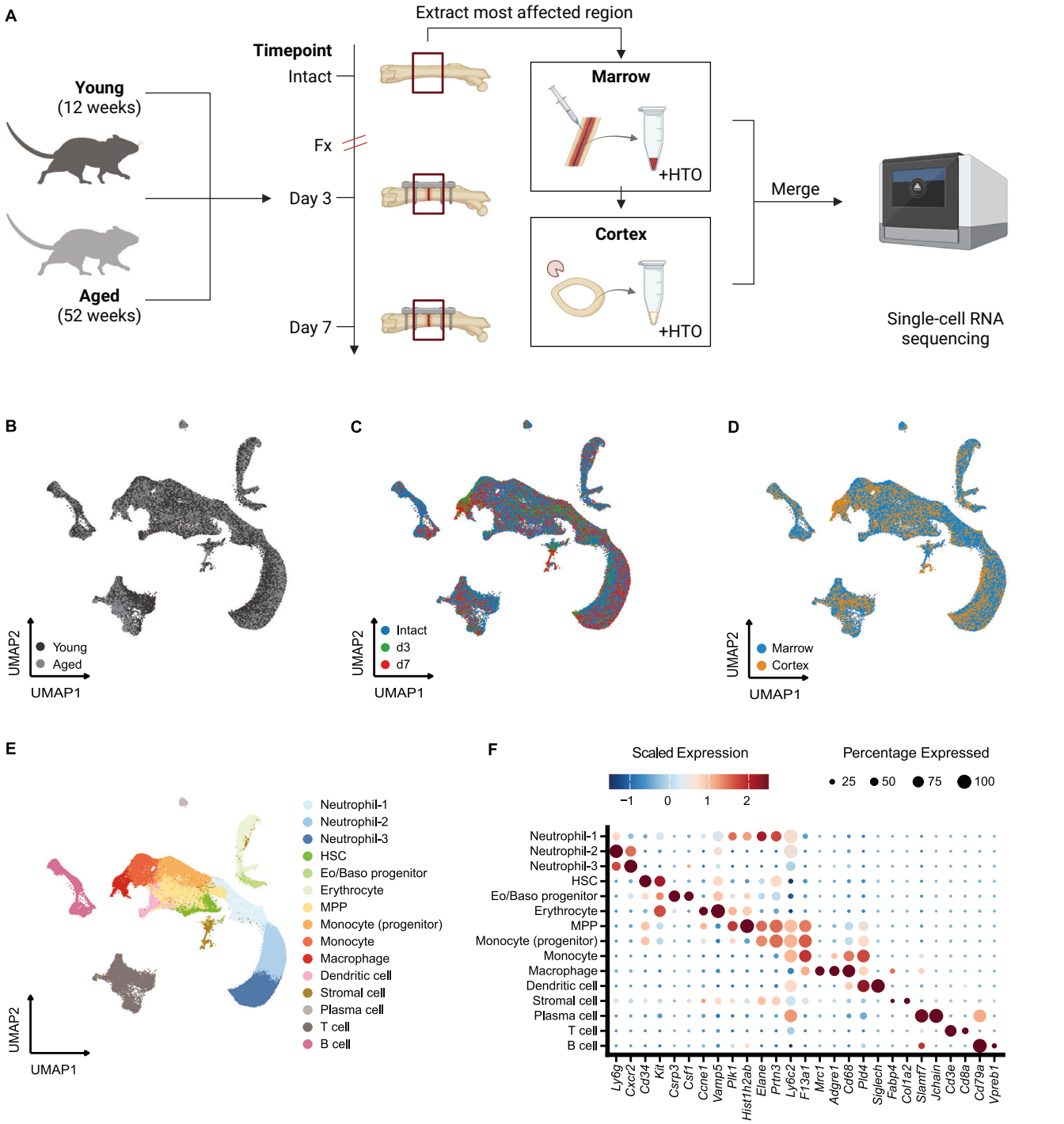

Fig. 2 | Experimental design and single-cell transcriptomic profiling of the fracture microenvironment. A Schematic overview of the in vivo fracture model and sample processing workflow. Young (12-week-old) and aged (52-week-old) mice underwent a standardized femoral osteotomy. Fracture callus tissue from the most affected region was harvested at d3 and d7 post-osteotomy, along with age-matched intact controls. Bone marrow was extracted by flushing the intramedullary canal, while cortical tissue was digested enzymatically. Hashtag oligonucleotide (HTO) labeling was used to retain sample identity prior to pooling and single-cell RNA sequencing. Schematic was created in BioRender; Noom, A. (2026) https://BioRender.com/j6ql5kd. **B-D** UMAP projections of 178,416 single cells derived from marrow and cortex samples across all conditions. Cells are color-coded by age group (**B**: young and aged), time point (**C**: intact, d3, and d7), and tissue origin (**D**: marrow and cortex). **E** Cell type annotation of identified clusters based on canonical gene expression markers reveals distinct immune and stromal populations, including innate and adaptive immune cells as well as stromal cells. **F** Dot plot showing the scaled expression of selected marker genes used for cluster annotation. Dot size indicates the percentage of cells expressing each gene per cluster, color intensity reflects average expression level. Source data are provided as a Source Data file.

To validate the selective recruitment of macrophages, neutrophils and stromal cells to the cortex following osteotomy, we next employed a 12-marker MELC panel to visualize cell distribution in bone tissue at days 3 and 7 post-osteotomy, with intact femurs from age-matched mice serving as controls (Fig. 3F, Supplementary Fig. 4). Consistent with our single-cell data, we did not detect an enrichment of either $CD68^{+}CD45^{+}$ cells (in their majority macrophages) or $Ly6G^{+}CD45^{+}$ cells (neutrophils) within 50 μm of the cortex in intact

https://doi.org/10.1038/s41467-026-77196-7

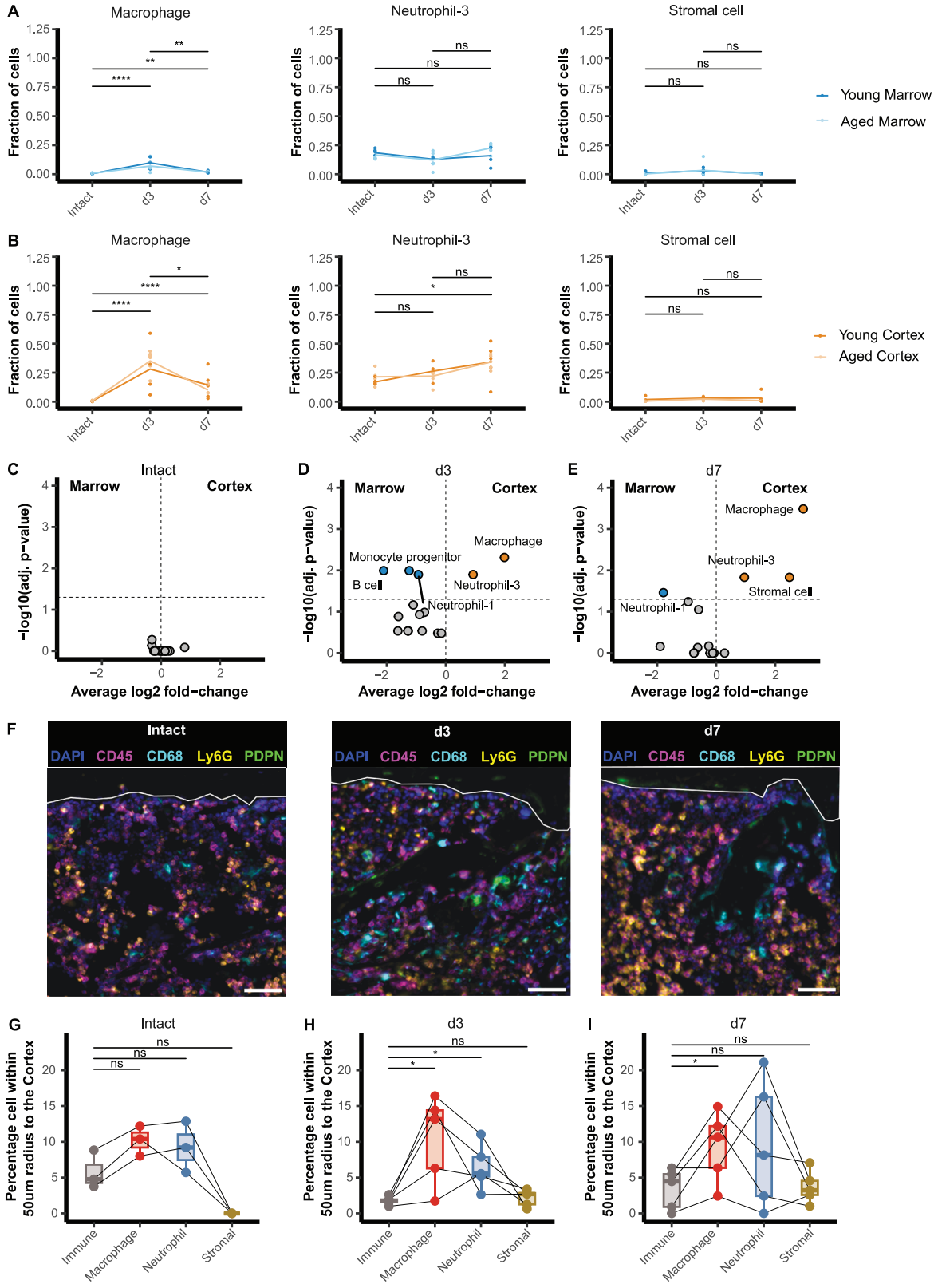

bones (Fig. 3G). However, at day 3, we observed an enrichment of $CD68^{+}CD45^{+}$ cells and $Ly6G^{+}CD45^{+}$ cells compared to other immune cells (Fig. 3H). By day 7, the enrichment of $CD68^{+}CD45^{+}$ cells remained significantly elevated (Benjamini-Hochberg-adjusted $p < 0.05$), whereas $Ly6G^{+}CD45^{+}$ cells only showed a modest abundance near the cortex (Fig. 3I). In contrast, $PDPN^{+}CD45^{-}$ cells (stromal cells) were sparsely distributed and remained at low frequency across all conditions (Fig. 3G–I), suggesting a more limited involvement in the early fracture response. Together, these data confirm the accumulation of distinct immune cell populations at the cortical interface (but not the marrow) during early fracture healing and support a potential role for spatially organized macrophage and

Fig. 3 | Temporal dynamics and spatial enrichment of macrophages, neutrophils and stromal cells at the cortical bone surface during early fracture healing. A–B Proportional abundance of macrophages, neutrophil-3 and stromal cells across time points (intact, d3 and d7) in marrow (**A**, blue) and cortex (**B**, orange). Each data point represents one biological replicate (Intact, $n = 10$; d3, $n = 10$; d7, $n = 9$). Lines connect the mean values within each age group across time points. *P* values were calculated using two-sided Wilcoxon rank-sum tests with Benjamini-Hochberg correction for multiple testing and can be found in the Source Data file; * $P < 0.05$, ** $P < 0.01$, *** $P < 0.001$, **** $P < 0.0001$; ns = not significant. **C–E** Volcano plots showing differential enrichment of cell populations between marrow and cortex at intact (**C**), d3 (**D**), and d7 (**E**). Log2 fold changes represent relative enrichment in cortex compared with marrow. Differential abundance was assessed using two-sided Wilcoxon rank-sum tests followed by Benjamini-Hochberg adjustment within each time point. Cell populations with adjusted $p < 0.05$ are labelled. **F** Immunofluorescence images of intact, d3, and d7 samples from young (12-week-old) mice showing cortical localization of $CD45^+CD68^+$ macrophages (cyan) and $CD45^+LY6G^+$ neutrophils (yellow) in proximity to the cortical bone surface (white line). Nuclei stained with DAPI (blue); CD45 (magenta) marks general immune cells; PDPN (green) indicates stromal cells; The line (white) indicates the cortical surface at the marrow site. Scale bar = 50 μm. **G–I** Quantification of spatial proximity of different cell types to the cortical bone surface, defined as the percentage of each population within a 50 μm radius from the cortex for intact (**G**), d3 (**H**) and d7 (**I**). Box plots display the median, interquartile range, and whiskers extending to the most extreme values within 1.5× the interquartile range. Individual data points represent biological replicates (intact, $n = 3$; d3, $n = 5$; d7, $n = 5$), and paired measurements from the same animal are connected by lines. Differences between cell populations were evaluated using paired one-sided Wilcoxon signed-rank tests; d3: immune-macrophage $P = 0.03$ and immune-neutrophil $P = 0.03$; d7: immune-macrophage $P = 0.03$; ns = not significant. Source data are provided as a Source Data file.

neutrophil activity in the early inflammatory and early osteoclast precursor response.

Fracture-associated *Spp1*^{hi} macrophages may act as cortex-specific precursors in osteoclastogenesis

Given the observed enrichment of macrophages at the cortical niche, where early osteoclastic activity is initiated, we next determined which macrophage subsets act as osteoclast precursors during bone regeneration. Therefore, we further isolated all cells annotated as monocyte progenitors, monocytes, and macrophages from the full scRNA-seq dataset and performed a subset-specific dimensionality reduction using UMAP visualization. By using Louvain clustering, we identified 6 distinct subpopulations (Fig. 4A, B), which showed a clear separation for cells derived from intact and fractured tissue (Fig. 4C).

Based on canonical marker gene expression and cross-referenced with established monocyte-derived macrophage and osteoclast differentiation datasets[19,35,36], these populations were annotated as monocyte progenitors, immature monocytes, mature monocytes, fracture-associated *Spp1*^{hi} macrophages, *Cd163*^{hi} macrophages as well as osteoclasts (Fig. 4D). Monocyte progenitors were defined by expression of *Sell* and high levels of *Ly6c2*, while immature monocytes expressed both *Ly6c2* and *Ccr2*, a chemokine receptor critical for monocyte recruitment to sites of injury. Mature monocytes were characterized by *Ccr2* in combination with *Cd74* and *Ciita*, genes associated with antigen presentation and inflammatory activation. Fracture-associated *Spp1*^{hi} macrophages showed strong expression of *Adgre1*, *Spp1*, *Cd14*, *C3ar1*, and *Mrc1*. Consistent with the description of *Spp1*^{hi} macrophage subsets from other injured organs, including fibrotic muscle[19], kidney[18], and lung[37], the fracture-associated *Spp1*^{hi} macrophages represent a damage-associated macrophage state. Their co-expression of inflammatory (*Cd14* and *C3ar1*)[19,38,39], reparative (*Mrc1*), and tissue-remodeling (*Spp1*)[16,40] indicates that they occupy a transitional inflammatory-reparative state responsive to environmental cues. *Cd163*^{hi} macrophages showed high expression of *Adgre1*, *Mrc1*, and *Cd163*, consistent with an anti-inflammatory role, whereas fracture-associated osteoclasts expressed canonical bone-resorptive genes *Acp5*, *Tnfrsf11a*, and *Ocstamp*, consistent with their role in matrix degradation and bone remodeling.

Having identified fracture-associated osteoclasts among our macrophage lineage subsets, we next performed pseudotime analysis to explore whether monocyte progenitors may give rise to fracture-associated osteoclasts through defined intermediate states following osteotomy. The resulting trajectory revealed a continuous progression originating from monocyte progenitors, transitioning through immature and mature monocytes, and branching into either *Cd163*^{hi} macrophages or osteoclasts as terminal fates (Fig. 4E). Interestingly, the fracture-associated *Spp1*^{hi} macrophages emerged as the key bifurcation point, marking a potential decision node between a reparative macrophage identity and an osteoclast fate. This observation extends previous models in which osteoclasts are thought to arise from multiple myeloid subsets, including monocytes and tissue-resident macrophages [22], by suggesting that an additional intermediate state may be involved during fracture healing. Collectively, these data provide evidence that fracture-associated *Spp1*^{hi} macrophages represent a transitional macrophage state which, in the context of bone healing, has the potential to differentiate to osteoclasts at the fracture site.

To functionally assess osteoclast differentiation capacity along the inferred myeloid trajectory, we performed osteoclastogenesis assays where we plated equal numbers of cells using flow-sorted myeloid populations. Based on marker expression patterns identified in our single-cell dataset, we isolated two phenotypically distinct populations representing successive stages along the trajectory: transitional *Spp1*^{hi} macrophages (identified as $CD14^+$ $F4/80^{lo}$) and *Cd163*^{hi} macrophages (identified as $CD163^{hi}F4/80^{hi}$) (Fig. 4D and Supplementary Fig. 5A, B). Upon stimulation with M-CSF and RANKL, *Spp1*^{hi} macrophages generated large, multinucleated TRAP-positive osteoclasts, demonstrating their osteoclast differentiation potential (Fig. 4F). In contrast, *Cd163*^{hi} macrophages formed very few osteoclasts. These findings indicate that *Spp1*^{hi} macrophages have a higher capacity to form osteoclasts, compared to other fracture-associated macrophage states, consistent with the notion that they represent a transitional macrophage state, which in the context of bone healing gives rise to fracture-associated osteoclasts.

To determine whether inflammatory conditions result in increased representation of *Spp1*^{hi} macrophages and/or increased osteoclast differentiation capacity, we performed these assays using macrophage subsets isolated from wild-type (*Tnf*$^{+/+}$) and *Tnf*$^{\Delta ARE/+}$ mice. In the latter, increased expression of TNF recapitulates chronic TNF-driven inflammation associated with enhanced osteoclastogenesis and pathological bone loss. Chronic TNF-driven inflammation did not significantly affect the relative osteoclastogenic efficiency of the examined subsets (Fig. 4F). Instead, inflammatory conditions primarily increased the abundance of osteoclast-competent precursor cells, without altering their per-cell differentiation potential (Supplementary Fig. 5C, Supplementary Data 4). Together, these findings support a model in which the representation of *Spp1*^{hi} macrophages with high osteoclastogenic capacity is increased under inflammatory conditions, while at the same time the representation of *Cd163*^{hi} macrophages, which have a lower capacity to form osteoclasts, is decreased.

To investigate whether the trajectories are reflected in the time kinetics of macrophage populations in vivo, we next quantified the relative proportions of each subset across timepoints and compartments following fracture (Supplementary Fig. 6A–D, Supplementary Data 5). In the marrow, both immature monocytes and *Spp1*^{hi} macrophages exhibit dynamic changes (Fig. 4G): a ~2-fold drop for the immature monocytes and an ~45-fold increase for *Spp1*^{hi} macrophages at day 3, both returning partially toward baseline by day 7. This pattern suggests a rapid recruitment and differentiation process, likely driven

https://doi.org/10.1038/s41467-026-77196-7

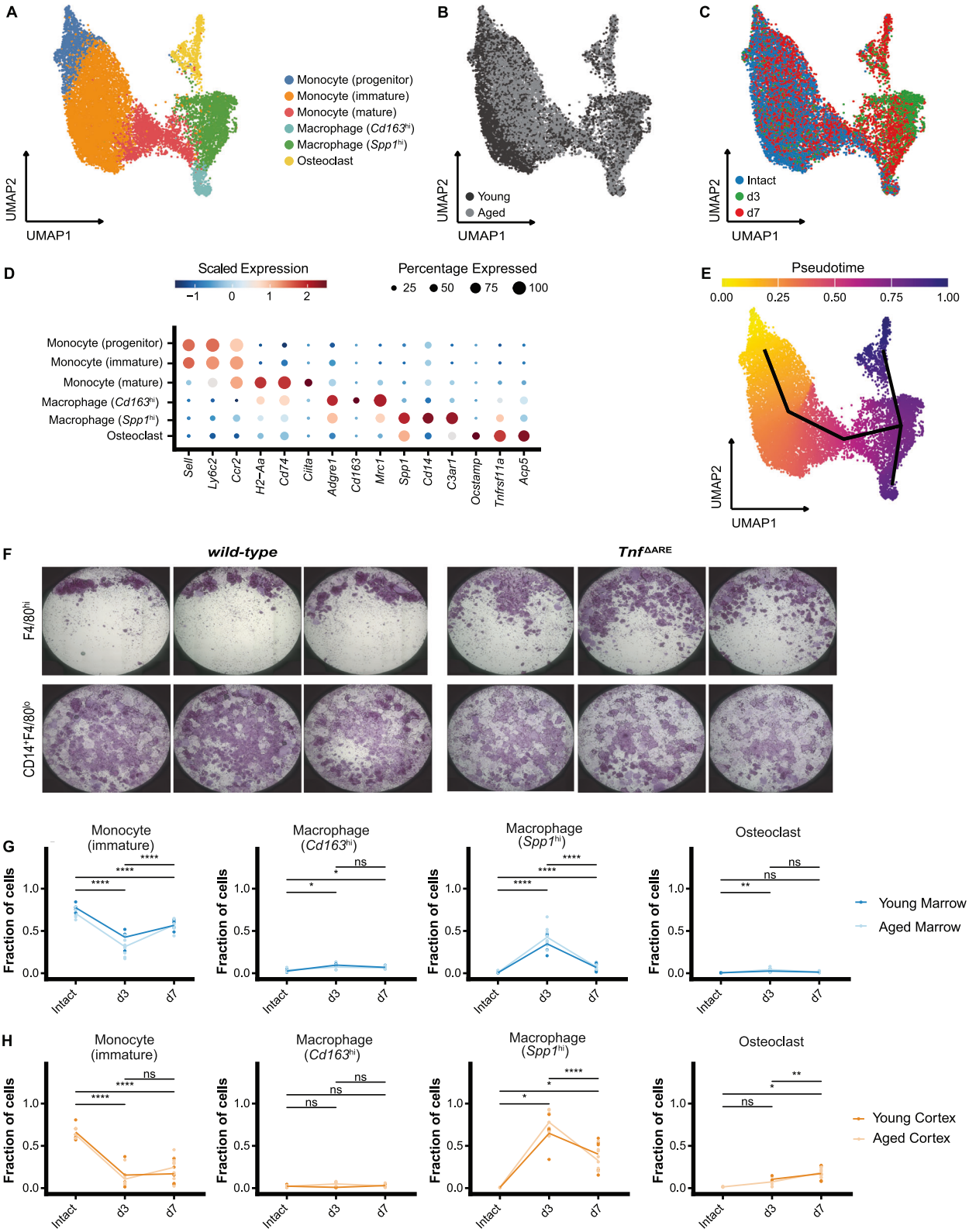

by injury cues. *Cd163*^{hi} macrophages and osteoclasts remained relatively stable over time, underscoring the unique temporal responsiveness of fracture-associated *Spp1*^{hi} macrophages during the early inflammatory phase.

At the cortex, similar trends but with greater amplitude were observed (Fig. 4H), with *Spp1*^{hi} macrophages increasing by ~75-fold by day 3. The early surge in fracture-associated *Spp1*^{hi} macrophages and the progressive increase in osteoclast numbers in the same niche point to a localized differentiation process, where *Spp1*^{hi} macrophages accumulate at the fracture site and give rise to osteoclasts in situ. The absence of such dynamics in contralateral controls reinforces the conclusion that these events are

Fig. 4 | Distinct temporal and tissue-specific differentiation trajectories of monocyte-derived macrophages during early fracture healing. A UMAP embedding of macrophage and monocyte lineage cells. **B–C** UMAP projections colored by age group (**B**: young and aged) and timepoint (**C**: intact, d3 and d7). **D** Dot plot of representative marker genes used to define each cluster, with dot size representing percentage of expressing cells per cluster and color indicating scaled expression. **E** Pseudotime projection of the macrophage lineage, with two distinct trajectories emerging from monocyte progenitors: one leading toward *Cd163*^{hi} macrophages in the marrow, and another via *Spp1*^{hi} macrophages toward osteoclast differentiation in the cortex. **F** Representative images of osteoclast differentiation assays from sorted macrophage populations under wild-type (*Tnf*$^{+/+}$) and *Tnf*$^{\Delta ARE/+}$ conditions. Upper panels show cultures derived from F4/80^{hi} cells, while lower panels represent CD14^{+}F4/80^{lo} macrophage-derived cultures. Osteoclast differentiation is indicated by TRAP-positive multinucleated cells. **G–H** Line plots showing changes in the fraction of each macrophage subtype over time (intact, d3, and d7) in marrow (**G**) and cortex (**H**). Data points represent biological replicates (intact, $n = 10$; d3, $n = 10$; d7, $n = 9$), and lines depict age group means. Comparisons across time points were performed using two-sided Wilcoxon rank-sum tests with Benjamini-Hochberg correction for multiple testing; $^{*}P < 0.05$, $^{**}P < 0.01$, $^{***}P < 0.001$, $^{****}P < 0.0001$; ns = not significant. Exact *P* values are provided in the Source Data file. Source data are provided as a Source Data file.

locally induced and fracture-specific (Supplementary Fig. 6E, Supplementary Data 5).

To further validate this compartmentalized differentiation, we assessed the tissue-specific distribution of these populations (Fig. 5A, Supplementary Fig. 6C, D). After osteotomy, the marrow remained rich in immature and mature monocytes, whereas fracture-associated *Spp1*^{hi} macrophages became enriched specifically in the cortex (Fig. 5B). Over time, *Cd163*^{hi} macrophages and osteoclasts were also enriched, but in distinct compartments: *Cd163*^{hi} in the marrow and osteoclasts in the cortex (Fig. 5B). This spatial segregation supports a model in which the cortical microenvironment selectively supports osteoclastogenesis, while the marrow sustains alternative fates.

To visualize the spatial layering of macrophage subsets during bone healing, we established a macrophage subset-specific marker panel to distinguish among monocytes, fracture-associated *Spp1*^{hi} macrophages, and *Cd163*^{hi} macrophages based on our single-cell data. We found *Cd68, Mrc1* and *Cd163* transcripts to be differentially expressed among the monocyte/macrophage populations (Fig. 5C). Using MELC, we confirmed the presence of a CD68^{+}CD206^{-}CD163^{-} population, consistent with monocytes, a CD68^{+}CD206^{+}CD163^{-} population, consistent with the fracture-associated *Spp1*^{hi} macrophage phenotype, and a CD68^{+}CD206^{+}CD163^{+} population, consistent with the CD163^{hi} macrophage phenotype, in our regions of interest (Fig. 5D).

We next assessed the frequency of CD68^{+} monocytes, CD68^{+}CD206^{+} macrophages and CD68^{+}CD206^{+}CD163^{+} macrophages within a radius of 50 μm of the cortex. Consistent with our single-cell results, we observed an enrichment of CD68^{+}CD206^{+} macrophages in comparison to the other myeloid populations after injury (Fig. 5E–G). CD68^{+}CD206^{+}CD163^{+} macrophages were also present in proximity to the cortex but constituted a lower percentage of their total population, indicating that while these cells contribute to the early fracture response, they are less dominant in this niche compared to CD68^{+}CD206^{+} macrophages. Together, this confirms that *Spp1*^{hi} macrophages not only occupy the osteoclast precursor position transcriptionally, but also CD68^{+}CD206^{+} macrophages, consistent with *Spp1*^{hi} macrophages in our single cell data, localize physically at the site of osteoclastogenesis.

To directly link spatial context to fate decisions, we performed a compartment-resolved pseudotime fate bias analysis (Fig. 5H). While early progenitors originated broadly, the transition toward osteoclasts occurred specifically within the cortex. *Spp1*^{hi} macrophages were concentrated at the bifurcation point, particularly within the cortical compartment, and gave rise to either osteoclasts when remaining in the cortex, or *Cd163*^{hi} macrophages when migrating to the marrow. Overall, these findings suggest an association between tissue compartment and fates where the niche might provide directional cues that resolve *Spp1*^{hi} cells into distinct fates, underscoring the spatial imprinting of osteoclastogenesis.

Osteoclastogenic programming of *Spp1*^{hi} macrophages is preserved with age

To explore how this differentiation program is influenced by age, we performed DEG and KEGG pathway analyses in monocyte-derived populations. Immature monocytes showed early expression of inflammation-associated genes at day 3, shifting toward maturation by day 7 (Supplementary Fig. 6F, Supplementary Data 5). Differential gene expression of fracture-associated *Spp1*^{hi} macrophages revealed that *Spp1*^{hi} macrophages at day 3 exhibited a pro-inflammatory and glycolytic gene signature, upregulating genes involved in immune activation and metabolic reprogramming (Fig. 6A). By day 7, their expression profile transitioned to oxidative phosphorylation and anti-inflammatory pathways as well as osteoclast differentiation, indicating a functional shift toward tissue remodeling and repair (Fig. 6B). These time-dependent changes confirm that fracture-associated *Spp1*^{hi} macrophages precede and likely enable the emergence of functional osteoclasts during early healing.

To further investigate the role of osteoclasts at different stages of fracture healing, we performed differential gene expression analysis to assess their functional state over time (Fig. 6D, E). We observed increased expression of *Acp5* and *Ctsk*, both of which are key markers of osteoclast activation and matrix degradation, by day 7 compared to day 3. While osteoclasts were already present on day 3, their transcriptional profile on day 7 suggested an enhanced resorptive function. TRAP staining further supports this transition, as osteoclast activity became more prominent near the cortical fracture site over time (Fig. 1), aligning with the observed transcriptional changes. These findings indicate that the cortical microenvironment supports early osteoclast presence but may also provide cues that shape their progressive specialization toward active bone resorption during later stages of healing.

Crucially, these transcriptional programs were largely preserved in aged mice (Fig. 6C, F, Supplementary Fig. 6F, G and Supplementary Fig. 7, Supplementary Data 5, 6). Direct cross-age pseudobulk comparisons at matched timepoints revealed only minimal transcriptional differences between young and aged mice in immature monocytes, fracture-associated *Spp1*^{hi} macrophages, and osteoclasts. The DEG comparisons further revealed that the myeloid cells followed similar activation and differentiation patterns across age groups. While the abundance of these populations may differ, their molecular programs remained intact. This suggests that age-related impairments in osteoclastogenesis are more likely due to altered microenvironmental signals rather than intrinsic cellular dysfunction.

Neutrophils may aid precursor recruitment with subtle age-sensitive niche changes

These findings underscore the central role of the tissue microenvironment in directing immune cell fate during fracture healing. To better understand the nature of these niche signals, we next examined the cellular components that dominate the early immune landscape at the fracture site. In addition to macrophages, Neutrophil-3 cells persisted in the cortical compartment beyond the acute phase (Fig. 3B, C), suggesting a more sustained and spatially anchored function. Given the known ability of neutrophils to influence macrophage polarization and osteoimmune signaling via cytokines such as IL-1β, IL-6, IFN-γ, and TNF-α[41], we hypothesized that neutrophils may contribute to the local

https://doi.org/10.1038/s41467-026-77196-7

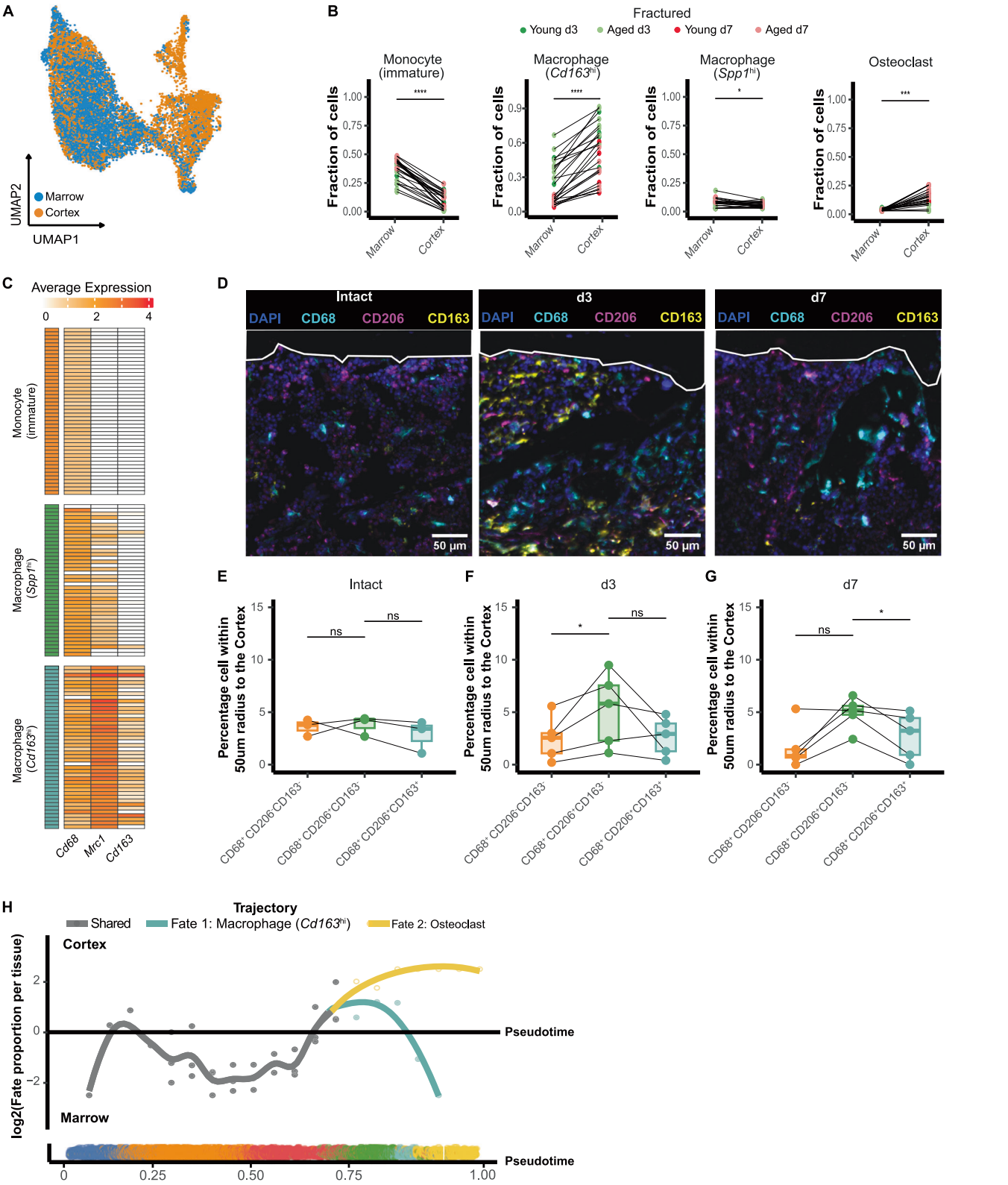

regulation of macrophage and osteoclast precursor recruitment and differentiation, including osteoclast formation.

To explore how neutrophils might contribute to niche-specific immune modulation during fracture healing, we investigated their molecular profile over time. Neutrophil-3 exhibited dynamic transcriptional changes over time (Fig. 7A, B). At day 3, they expressed pro-inflammatory and immune-activating genes such as *Tnf*, *Csf1*, and *Vegfa*, while by day 7, they upregulated *Mmp8* and genes linked to oxidative phosphorylation and ferroptosis, indicating a functional shift toward matrix remodeling and immune resolution. These temporally regulated states were maintained in aged mice, as gene expression profiles remained highly comparable across age groups (Fig. 7C). This

Fig. 5 | Compartment-specific fate bias of macrophage subtypes during early fracture healing. A UMAP embedding of macrophage/monocyte lineage cells from all samples colored by tissue origin (marrow: blue; cortex: orange), revealing spatial segregation of macrophage subtypes. **B** Paired quantification of monocyte and macrophage subtype distributions across marrow and cortex for young and aged mice in fractured conditions (d3 and d7 post-osteotomy). Individual data points represent biological replicates, and paired samples from the same replicate are connected by lines. Tissue-specific differences were assessed using paired one-sided Wilcoxon signed-rank tests; * $P < 0.05$, ** $P < 0.01$, *** $P < 0.001$, **** $P < 0.0001$; ns = not significant. The P values can be found in the source data file. **C** Heatmap showing normalized expression of key markers across macrophage subsets, confirming phenotype-specific gene expression signatures. **D** MELC images from young (12-week-old) mice showing cortical localization of $CD68^+CD206^-CD163^-$ monocytes, $CD68^+CD206^+CD163^-$ macrophages, and $CD68^+CD206^+CD163^+$ macrophages. DAPI (blue) marks nuclei; CD68 (cyan) marks general myeloid cells; CD206 (magenta) and CD163 (yellow) identify functionally distinct subsets. White lines indicate the cortical bone surface; The line (white) indicates the cortical surface at the marrow site. Scale bar = 50 μm. **E**–**G** Quantification of macrophage subset localization within 50 μm of the cortical surface for intact (**E**), d3 (**F**) and d7 (**G**) samples. Box-and-whisker plots show the median (centre line), interquartile range (box limits), and whiskers extending to the most extreme values within 1.5× the interquartile range. Individual data points represent biological replicates (intact, $n = 3$; d3, $n = 5$; d7, $n = 5$), and paired observations from the same animal are connected by lines. Significance was evaluated using paired one-sided Wilcoxon signed-rank tests; d3: $P = 0.031$; d7: $P = 0.031$; ns = not significant. **H** Pseudotime-aligned plot showing inferred differentiation trajectories of monocyte/macrophage lineage across pseudotime. Log_2-transformed fate probabilities per tissue are shown along the trajectory. Cells are assigned to one of three inferred fates: shared (gray), *Cd163*^{hi} macrophages (cyan), or osteoclasts (yellow). Colored points below the plot indicate cell-wise trajectory labeling across pseudotime. Source data are provided as a Source Data file.

suggests that neutrophil maturation and function are preserved with aging, and that their role in shaping the cortical immune niche remains intact.

Although neutrophil and macrophage activation programs remained largely intact with aging, we next asked whether their communication within the cortical niche was similarly preserved. Ligand–receptor analysis of cortex-enriched innate immune populations revealed that Neutrophil-3 and *Spp1*^{hi} macrophages formed the dominant cell–cell interaction axis during early fracture repair (Fig. 7D). Mapping of ligand–receptor pairs showed a dense signaling network involving key mediators such as *Cxcl2*, *Spp1*, *Tnf*, and *Ccl* family members, linking this axis to both inflammatory recruitment and immune resolution (Fig. 7E). GO enrichment further highlighted strong involvement of chemotaxis, cytokine signaling, and regulatory immune pathways (Fig. 7F), suggesting that these two populations jointly orchestrate niche dynamics. Together, these findings highlight neutrophil–macrophage communication as a prominent feature of the early spatial immune landscape during bone healing.

We then examined how these interactions evolve over time (Fig. 7G). Interestingly, both *Cxcl2*–*Cxcr2* and *Spp1*–*Cd44* signaling remained consistently enriched within the cortical microenvironment across timepoints, suggesting a sustained role in neutrophil recruitment, macrophage activation, and extracellular matrix remodeling[42,43]. However, a temporal shift was apparent in other interactions, with chemotaxis signaling being more dominant at day 3, such as *Ccl3-Ccr1*, *Ccl6-Ccr1* and *Ccl9-Ccr1* as well as *Fn1-Cd44*, while immune regulation pathways gained prominence by day 7, including *Cd80-Cd274*, *Igf1-Igf1r* and *Jag1-Notch2*. Although not directly instructing cell fates, such interactions may reflect mutual priming with neutrophils and macrophages influencing each other's maturation and potentially guiding macrophages toward osteoclastogenic trajectories. Moreover, this shift suggests that the cortical microenvironment serves as a structured immune niche where neutrophils and macrophages organize their signaling in a time-dependent manner, coordinating the transition from inflammatory recruitment to immune resolution.

Importantly, when comparing young and aged mice, we found that the core signaling framework remained intact (Fig. 7H). However, several interactions showed subtle shifts in their relative enrichment. For example, *Ccl4-Ccr5* signaling seems to be more present in age cortical compartments, potentially reflecting altered precursor recruitment dynamics[44]. Moreover, Thrombospondin-1 (*Thbs1*)-associated interactions, which are linked to matrix remodeling[45–47], were more prominent in aged mice. These differences occurred despite largely preserved transcriptional states in both neutrophils and macrophages, pointing to a subtly rewired cell-cell communication with age.

Pre-osteoblasts shape an osteoclast-supportive niche at young cortical bone

The cortical microenvironment is, however, not solely shaped by immune cells. Stromal cells, including osteolineage and mesenchymal stromal populations, are well-known sources of growth factors, cytokines, and extracellular matrix components that govern immune cell positioning, survival, and differentiation[48]. To further dissect how the non-hematopoietic compartment contributes to fracture niche regulation and whether this is altered with age, we next focused on the transcriptional dynamics of stromal cells across compartments and timepoints.

Using clustering and canonical marker genes, we identified two broad populations within the stromal compartment: endothelial cells and pre-osteoblasts (Fig. 8A–D). While endothelial cells expressed vascular markers such as *Pecam1*, *Emcn*, and *Cdh5*, the pre-osteoblast population was markedly heterogeneous (Fig. 8E). Subsets expressing *Vim*, *Col1a1*, *Pdpn*, and *Acta2* likely represent fibroblast- or pericyte-like cells, while others expressed *Acan*, *Sp7*, and *Gpam*, consistent with osteochondral and adipogenic potential. This compositional diversity indicates that multiple stromal lineages coexist in the fracture niche and may functionally support immune coordination and bone repair.

We next applied gene module scoring to assess the activity of predefined mesenchymal differentiation programs. Pre-osteoblasts from young mice showed higher scores for progenitor-like programs (Fig. 8F), indicating a more robust regenerative progenitor pool. Importantly, osteogenic and chondrogenic programs remained relatively comparable between groups (Fig. 8G, H), while adipogenic signatures were subtly but consistently lower in young mice (Fig. 8I), suggesting a more osteoblast-supportive lineage bias. This balance may enhance the capacity of pre-osteoblast in young mice to contribute to a regenerative fracture environment.

We also assessed whether this regenerative bias was reflected in the expression of niche-regulatory signals essential for immune cell function and osteoclastogenesis (Fig. 8J). Pre-osteoblasts from young mice showed higher expression of key factors including *Csf1*, *Tnfsf11* (RANKL), *Cxcl12*, *Wnt5a*, and *Il6*, which collectively mediate myeloid recruitment, survival, and osteoclastogenesis. This elevated niche signaling was most pronounced in the fractured cortical tissue, where young mice maintained higher module scores compared to aged mice. Together, these findings suggest that pre-osteoblasts in young mice provide a more supportive niche environment for osteoclastogenesis during early fracture healing.

Discussion

Fracture healing is a tightly regulated regenerative process that relies on coordinated interactions between immune and stromal cell

https://doi.org/10.1038/s41467-026-77196-7

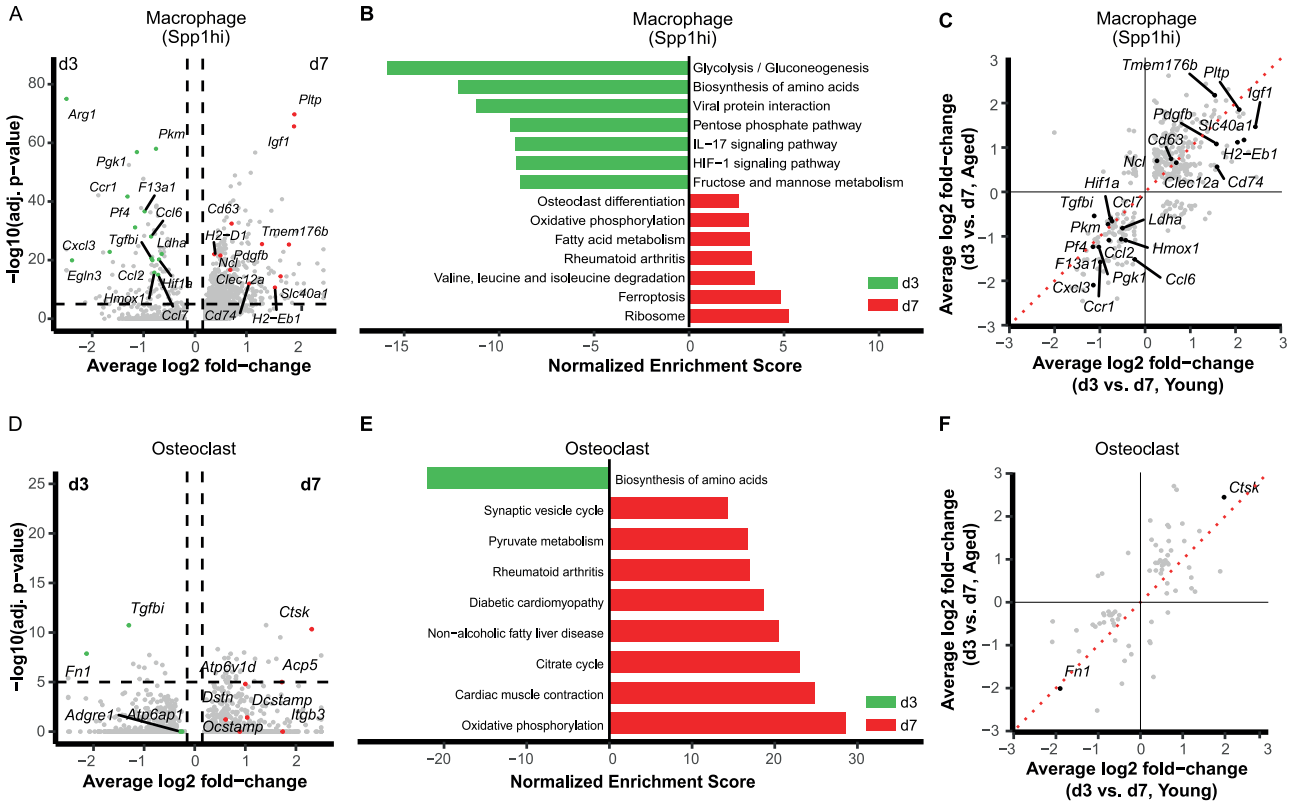

Fig. 6 | Temporal and age-comparative transcriptomic profiling of *Spp1*^{hi} macrophages and osteoclasts during fracture healing. A Volcano plot showing differentially expressed genes (DEGs) in *Spp1*^{hi} macrophages between d3 and d7 post-osteotomy. Genes labeled in green indicate significant upregulation at d3; genes in red are upregulated at d7. Differential expression analysis was performed using two-sided Wilcoxon rank-sum tests with Benjamini-Hochberg adjustment for multiple testing. **B** KEGG pathway analysis of DEGs in *Spp1*^{hi} macrophages, comparing d3 (green) and d7 (red) based on normalized enrichment scores. **C** Comparative DEG plot for *Spp1*^{hi} macrophages showing average $\log_2$ fold change values between d3 and d7 in young versus aged mice. Highlighted genes indicate consistent regulation across age. **D** Volcano plot showing DEGs in osteoclasts between d3 (green) and d7 (red) post-osteotomy. Statistical significance was assessed using two-sided Wilcoxon rank-sum tests, and *p*-values were adjusted using the Benjamini-Hochberg procedure. **E** KEGG pathway analysis of DEGs in osteoclasts comparing d3 (green) and d7 (red) based on normalized enrichment scores. **F** Comparative DEG plot for osteoclasts, plotting average $\log_2$ fold change values for young (x-axis) and aged (y-axis) mice. Black dots represent genes consistently regulated across age. Source data are provided as a Source Data file.

populations in a localized and spatially distinct manner. Although osteoclasts are classically associated with late-stage remodeling, evidence points to their very early appearance in bone regeneration and thus an orchestrated recruitment from their precursors directly at the start of healing. However, the cellular origins and regulation of osteoclastogenesis during this early bone repair phase remain incompletely understood. The goal of this study was therefore to identify how tissue microenvironments define this early process of bone healing by potentially regulating osteoclastogenesis, eventually altered in aging.

By combining single-cell RNA sequencing with spatial imaging, we reveal that within the early inflammatory phase of secondary fracture healing, the cortical niche serves as the primary site of innate immune activation, tissue remodeling, macrophage clearing of tissue debris, and osteoclastogenesis, while the bone marrow retains its role as a hematopoietic reservoir[2]. This spatial organization of macrophage and osteoclast healing responses was largely preserved in aged animals, indicating that the compartmental framework of fracture repair remains intact with aging. However, despite this preserved structure, we observed an instant increase in early osteoclast number and activity at the fracture site in young mice, distinct from a known increase in baseline osteoclast activity and systemic bone resorption in aged mice[49,50]. This apparent paradox underscores a key distinction between chronic, homeostatic changes with age in bone turnover and the tightly regulated, injury-induced osteoclastogenesis required for regeneration.

To address this discrepancy, we next aimed to identify transcriptional states that may represent osteoclast precursors during early healing. Consistent with reports in other injured tissues, such as the muscle[19], lung[37], kidney[18], and even bone, our analysis also revealed a distinct *Spp1*^{hi} macrophage population. In the unique context of fracture healing, we were able to resolve features of the fracture-associated *Spp1*^{hi} macrophage state that have not been defined previously in bone: its differentiation trajectory, dynamic emergence during early timepoints in the healing process, enrichment at the cortex, and its position at the transition toward osteoclast identity. Trajectory analysis demonstrated that fracture-associated *Spp1*^{hi} macrophages form a key intermediate between *Ly6C*^{hi} monocytes, reparative *Cd163*^{hi} macrophages, and osteoclasts. Their mixed M1/M2-like transcriptional profile indicates responsiveness to local cues produced in the cortical microenvironment. Their upregulation of osteoclast-associated transcripts is in agreement with their capacity to form osteoclasts ex vivo. The accumulation of *Spp1*^{hi} macrophages at the cortex, coincident with rising osteoclast numbers, suggests that their differentiation is spatially instructed by the bone healing microenvironment rather than intrinsic. Notably, this transitional state was preserved in aged mice, even though downstream osteoclastogenic output was diminished, suggesting that age primarily alters the niche rather than the precursor state itself.

Our data point to neutrophils as essential catalysts to this macrophage-driven kick-start in the cortical niche at the onset of healing. Traditionally seen as short-lived inflammatory cells,

https://doi.org/10.1038/s41467-026-77196-7

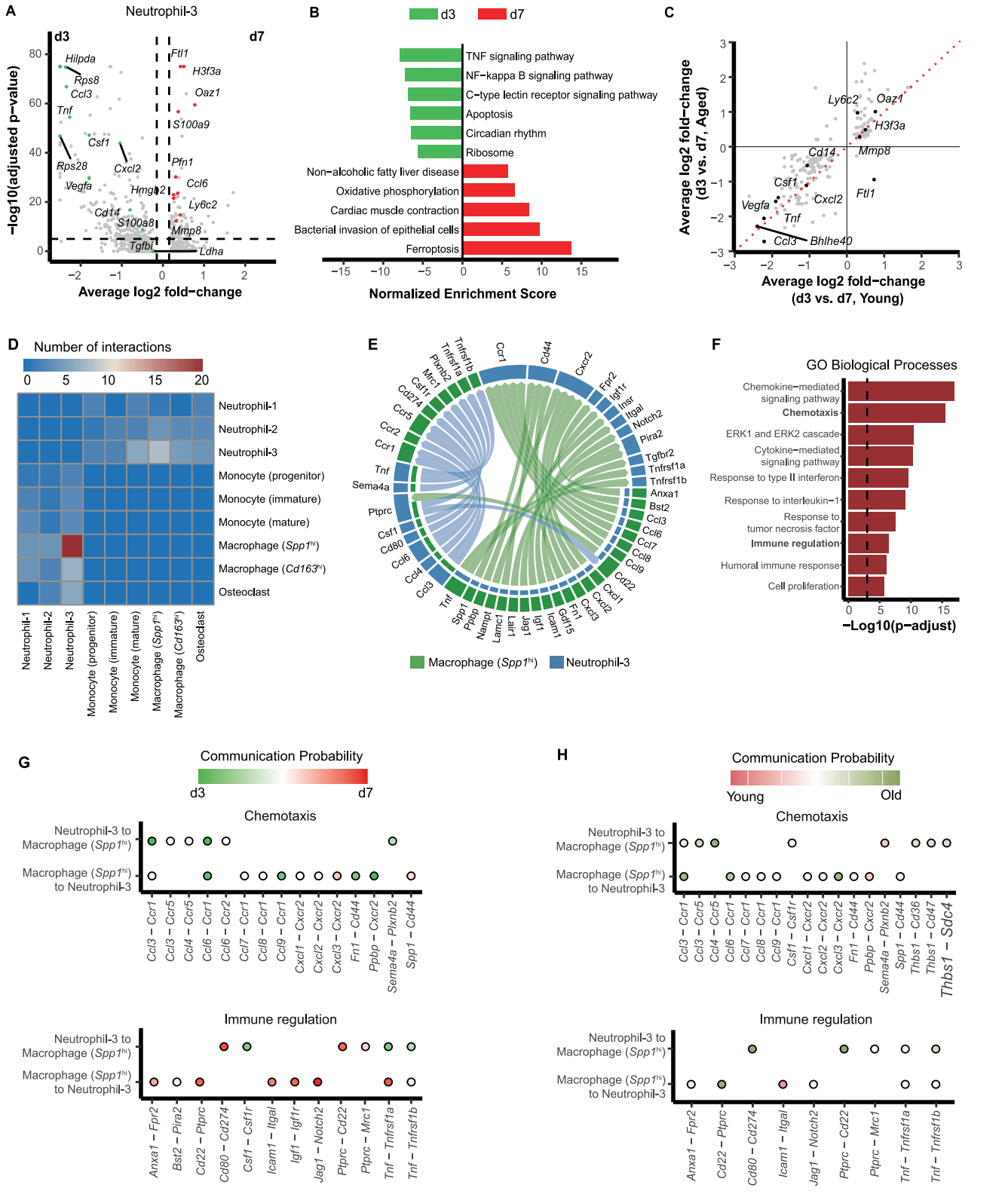

neutrophils persisted in the cortical compartment, transitioning toward matrix-remodeling states. Recent studies have highlighted neutrophil persistence in tissue repair, particularly wound healing and fibrosis models[51–53], where they influence macrophage activity and ECM remodeling. Similar findings in injury models suggest that dysregulated neutrophil clearance can lead to chronic inflammation[54], raising the possibility that neutrophil retention in the cortical niche must be tightly regulated to prevent prolonged inflammation. Their predicted ligand–receptor interactions with *Spp1*^{hi} macrophages, particularly via *Cxcl2*–*Cxcr2* and *Spp1*–*Cd44*, suggest that, also during fracture healing, neutrophils and macrophages operate in close coordination, shaping each other's activation and positioning within

Fig. 7 | Temporal and directional immune communication between Neutrophil-3 and *Spp1*^{hi} macrophages during fracture healing. A Volcano plot showing differentially expressed genes (DEGs) in Neutrophil-3 cells between d3 and d7 post-osteotomy. Genes significantly upregulated at d3 or d7 are highlighted in green and red, respectively. Differential expression was evaluated using two-sided Wilcoxon rank-sum tests with Benjamini-Hochberg correction for multiple testing. **B** KEGG pathway analysis of DEGs from **A**, comparing d3 (green) and d7 (red) using normalized enrichment scores. **C** Comparative DEG analysis in Neutrophil-3 cells between young and aged mice, showing average $\log_2$ fold change for each gene at d3 vs. d7. **D** Heatmap displaying the number of identified ligand-receptor pairs between neutrophil and macrophage subtypes across directions and time points. Cell color indicates interaction count; columns represent sender cells, whereas rows represent receiver cells. **E** Circos plot visualizing predicted ligand-receptor interactions between Neutrophil-3 and *Spp1*^{hi} macrophages, stratified by communication direction. **F** Gene ontology (GO) enrichment analysis of ligand-receptor pairs expressed by Neutrophil-3 and *Spp1*^{hi} macrophages, highlighting processes such as chemotaxis and immune regulation. Significantly enriched GO terms were identified using Benjamini-Hochberg-adjusted *p*-values. **G** Dot plots showing temporally resolved ligand-receptor interactions at d3 and d7 between Neutrophil-3 and *Spp1*^{hi} macrophages, grouped by GO biological process: chemotaxis (top row) and immune regulation (bottom row). Dot size reflects interaction score; color represents the dominant time point (green: d3; red: d7). **H** Dot plots showing ligand-receptor interaction profiles in young and aged mice, across both communication directions and timepoints, grouped by GO biological process: chemotaxis (top row) and immune regulation (bottom row). Dot size reflects interaction score; color represents the dominant age group (red: young; green: aged). Source data are provided as a Source Data file.

the niche. Although neutrophil activation programs were preserved in aged mice, age-specific changes in signaling interactions emerged, such as *Ccl4–Ccr5* and Thbs1-mediated pathways. These subtle alterations may reduce the functional relay between neutrophils and macrophages, delaying the osteoclastogenic transition despite preserved cellular states.

While immune-immune interactions coordinate early inflammation and precursor positioning, pre-osteoblasts ultimately provide the niche infrastructure and molecular cues, such as *Csf1*, *Tnfsf11*, and *Wnt5a*, required to initiate osteoclast differentiation[55–59]. In our study, these signals were more prominently expressed in young mice, particularly within the fractured cortical compartment, suggesting a more responsive stromal niche early in healing. Gene module analysis further revealed that pre-osteoblasts in young mice exhibited stronger progenitor-like programs and lower adipogenic expression, consistent with a regenerative lineage bias[7,60]. These findings suggest that pre-osteoblasts in young mice actively provide the niche cues necessary to support osteoclast precursor maturation, including signals that coordinate with recruited macrophages and neutrophils. This early stromal activity appears reduced in aged tissue, where the same cues are less effectively engaged following injury. In this context, the ability of the young stromal niche to initiate early remodeling emerges as a second key determinant of regenerative success. Therapeutically enhancing or mimicking these stromal signals may offer a targeted strategy to promote osteoclast function during fracture healing in aging bone.

Several limitations of this work should be acknowledged. First, although our data position fracture-associated *Spp1*^{hi} macrophages upstream of osteoclasts in transcriptional space and spatially associate them with early osteoclasts, a finding which we functionally validated with ex vivo osteoclastogenesis assays, we cannot yet establish a direct precursor-product relationship. Lineage tracing using fate-mapping or targeted depletion will be required to determine whether *Spp1*^{hi} macrophages directly contribute to the osteoclast pool during fracture healing. Second, our single-cell RNA sequencing relied on tissue dissociation and may therefore underrepresent fragile or spatially embedded cells. Finally, although our analyses highlight age-related changes in niche activity rather than intrinsic cellular defects, additional work integrating functional assays or in situ perturbations will be needed to better define how aging alters the coordination between immune and stromal compartments during early fracture healing.

In conclusion, we demonstrate that early osteoclastogenesis from distinct sets of macrophages is not solely a function of precursor identity but is critically governed by spatially organized niches and their signals involving specific macrophage subsets, neutrophils, and stromal cells. Aging does not abrogate the potential for osteoclast differentiation but alters or disrupts the niche required to support it. Notably, we identify *Spp1*^{hi} macrophages as early, cortex-restricted transitional cells that defy classical M1/M2 polarization and emerge in close coordination with neutrophils. This co-localized immune module forms a pre-regenerative microenvironment that initiates remodeling cascades from the earliest stages of healing. Its spatial restriction to the cortical compartment, and its absence in intact tissue, underscores its specificity and potential as a checkpoint for successful regeneration. These findings provide a new conceptual framework for how tissue context shapes immune function at the very early start of regeneration, and highlight differences in aging that may be conceptually addressed to improve healing across aging.

Methods

Animal Model

Female C57BL/6NRj mice were purchased from Janvier at ages 10 and 26-32 weeks, and were used at ages 12 and 52 weeks for the mouse osteotomy model. *Tnf*$^{\Delta ARE/+}$ mice were generated[61] and kindly provided by George Kollias. All animals were imported with a health certificate and kept under obligatory hygiene standards that were monitored according to the FELASA standards. The mice were kept under specific pathogen-free (SPF) housing. Food and water were available *ad libitum*, and animals were maintained in a temperature-controlled environment with 45–50% relative humidity and a 12 hours light/dark cycle. All experiments were carried out with ethical permission according to the policies and principles established by the Animal Welfare Act, the National Institutes of Health Guide for Care and Use of Laboratory Animals, and the National Animal Welfare Guidelines, the ARRIVE guidelines, and were approved by the local legal representative animal rights protection authorities (G0012/22; Landesamt für Gesundheit und Soziales Berlin).

Mouse Osteotomy as a model to study bone regeneration

Secondary bone regeneration was studied with a mouse osteotomy model. The osteotomy was performed under isoflurane anesthesia. The anesthesia was given to the mouse through a mask with an isoflurane-oxygen mixture. Before the surgery, mice were subcutaneously injected with Buprenorphine (analgesic) and Clindamycin (antibiotic), and eye ointment was applied to protect the eyes. The surgical area was shaved, and the surgery was performed on a heating pad (37 °C). The osteotomy was performed as previously published[7,33]. To summarize, after shaving the surgical area of the left femur, the skin was opened, and the femur was carefully exposed. An external rigid fixator (MouseExFix, RISystem, Davos, Switzerland) was mounted on the femur, and the osteotomy was performed with a gap size of 0.7 mm. Afterwards, the wound was closed, and Tramadol was added to the drinking water for 3 days. Animals were sacrificed 3, 7, and 21 days post-surgery through intraperitoneal injection with a mixture of Medetomidine and Ketamine to induce deep anesthesia, followed by a cervical dislocation.

Bone tissue sample preparation for single-cell RNA sequencing

The femurs were carefully excised and stored in ice-cold phosphate-buffered saline (PBS) supplemented with 2% fetal calf serum (FCS) to preserve cellular viability during transportation. For bone marrow

https://doi.org/10.1038/s41467-026-77196-7

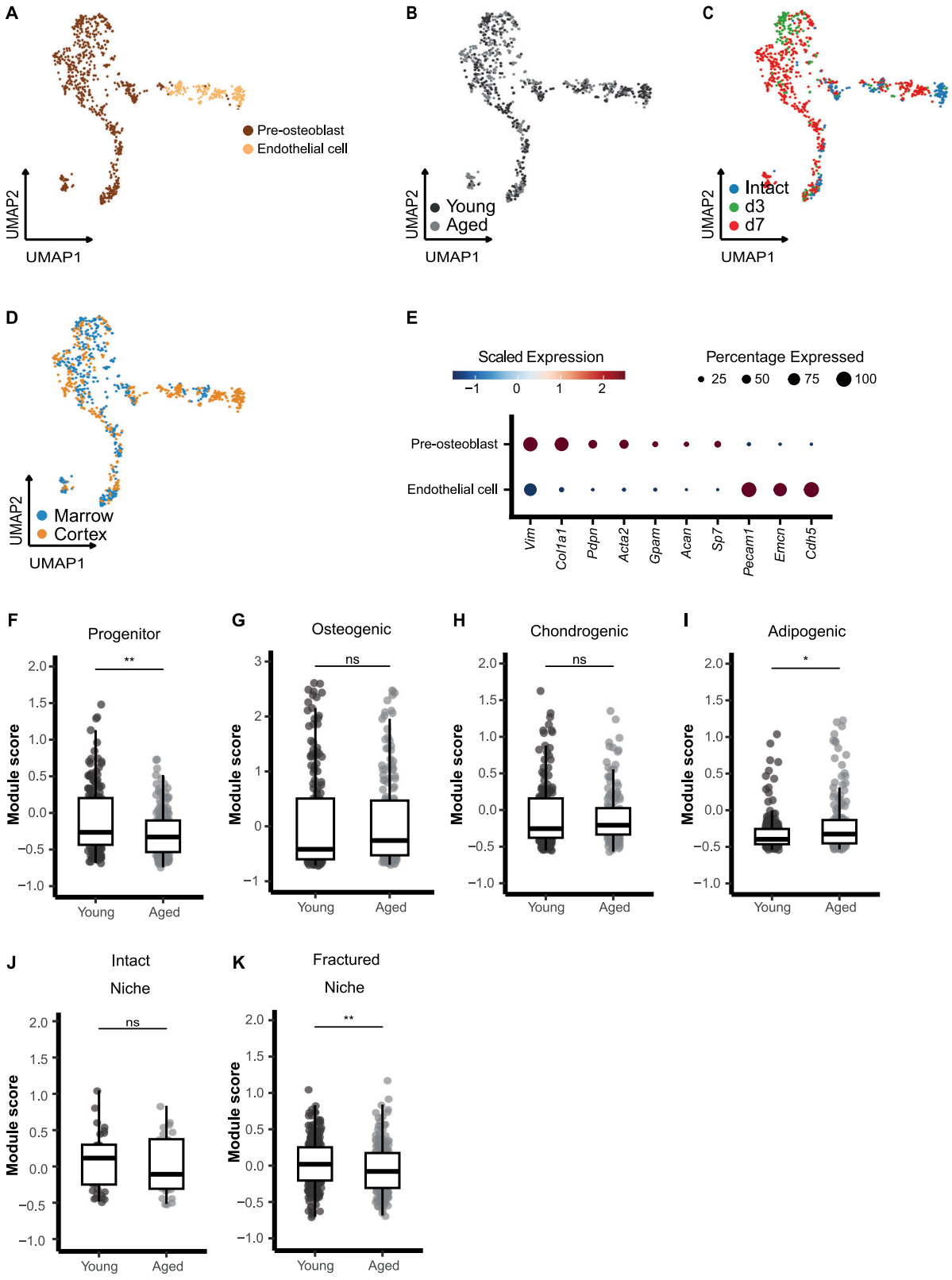

isolation, the femurs were sectioned from inner pin to inner pin, followed by flushing the marrow out of the cavity. The resulting cell suspension was filtered through a cell strainer, and the red blood cells were lysed with ACK lysis (ThermoFischer Scientific). The reaction was neutralized by adding PBS + FCS solution. To isolate cells from the cortical bone, the bone cavities were washed three times with 10 mL digestion medium (1 mg/mL of each collagenase IV and dispase II in Hanks' balanced salt solution; all from Gibco) for 30 min at 37 °C in a water bath. Following incubation, the digest was filtered through a cell strainer to obtain a cell suspension suitable for further analysis.

Fig. 8 | Age-associated changes in progenitor and differentiation potential of pre-osteoblasts. A–D UMAP embedding of stromal cells subclustered into pre-osteoblasts and endothelial cells, shown by cell identity (**A**), age group (**B**), time-point (**C**) and tissue origin (**D**). **E** Dot plot showing scaled expression and percentage of expressing cells for representative marker genes across the identified stromal subsets, confirming cell type identity. **F–I** Module scores for transcriptional programs related to progenitor identity (**F**), osteogenic (**G**), chondrogenic (**H**) and adipogenic (**I**) differentiation in young and aged mice. Box plots show the median (centre line), interquartile range (box limits), and whiskers extending to the most extreme data points within 1.5× the interquartile range. Individual data points represent single cells. Cells were derived from young (d7, $n = 4$) and aged (d7, $n = 5$) animals. Statistical comparisons between young and aged groups were performed using unpaired one-sided Wilcoxon rank-sum tests; progenitor score: $P = 0.031$; adipogenic score: $P = 8{\times}10^{-8}$; ns = not significant. **J–K** Comparison of osteoclastic niche signaling module scores between young and aged mice in intact (**J**) and fractured (**K**) tissues. Box plots show the median (centre line), interquartile range (box limits), and whiskers extending to the most extreme data points within 1.5× the interquartile range. Individual data points represent single cells. Cells were derived from young (Intact, $n = 5$; d7, $n = 4$) and aged (Intact, $n = 5$; d7, $n = 5$) animals. Statistical comparisons between young and aged groups were performed using unpaired one-sided Wilcoxon rank-sum tests; fractured: $P = 0.0002$; ns = not significant. Source data are provided as a Source Data file.

Single-cell RNA Sequencing – 10x Genomics

For scRNAseq using 10x Genomics, marrow and cortical bone cells were processed as described earlier [31]. Each compartment was stained with Cell Hashing antibodies following the CITE-seq protocol. After staining and washing, a final concentration of ~1000 cells/uL, was loaded into the 10x Genomics Chromium Controller for Single Cell 3′ v3 workflow, according to the manufacturer's instructions.

In brief, reverse transcription and library construction were carried out per the 10x Genomics protocol. Total cDNA synthesis involved 12–14 amplification cycles, resulting in final cDNA yields ranging from approximately 1 ng/uL and 64 ng/uL. The 10x Genomics sequencing libraries were constructed as described and sequenced on an Illumina NextSeq 500. Sequencing was performed with paired-end read lengths of 26 bp for Read 1 and 58 bp or 98 bp for Read 2.

The raw sequencing reads were processed using Cell Ranger Count (v7.1.0) (10X Genomics), which involved alignment to the mouse genome (mm10) and the generation of count matrices containing both mRNA and HTO read counts. The resulting count data were then analyzed following standard processing pipelines in Seurat[62] (v.5.1.0). Cells with fewer than 500 detected genes, more than 10% mitochondrial gene expression, or identified multiplets were excluded. Cell cycle scores were computed using the CellCycleScoring function, and data were normalized and scaled using NormalizeData and ScaleData functions, which regress out mitochondrial content, cell cycle phase score, and RNA feature counts. Data integration across compartments was performed using Harmony[63] (v1.2.3). Dimensionality reduction was carried out using principal component analysis (PCA), with the number of PCs determined by elbow plot inspection. Two-dimensional embeddings were generated using UMAP. Clusters were identified via Louvain clustering (FindClusters), and differential gene expression was assessed using the FindMarkers function. Iterative subclustering was applied to refine immune populations, and clusters with gene signatures consistent with low-quality cells or contaminating populations were removed.

Bone sample preparation for (immuno)histological analysis

Osteotomized femurs were cryo-embedded according to the Kawamoto method. The harvested bones were directly fixed in 4% paraformaldehyde for 2 h at 4 °C. They were then transferred to a series of increasing sucrose solutions (10%, 20%, and 30%) for cryoprotection, with each step lasting 24 hours at 4 °C. After cryoprotection, bones were embedded in SCEM media (SectionLab, Yokohama, Japan) using precooled n-hexane. Embedded bones were stored at −80 °C until sectioning.

For sectioning, the cryo-embedded blocks were mounted onto a cryotome sample holder using Tissue-Tek O.C.T. Compound (Sakura, #4583). Sections of 7 um thickness were cut using a Leica cryostat (Leica), and transferred onto Kawamoto tape (Section lab, #C-FP096). These sections were mounted on a glass slide and fixed with Tesafilm strips for further processing.

Histomorphometry analysis

For histomorphometry analysis, Movat Pentachrome staining was performed on bone sections. The sections were stained sequentially with alcian blue (8GS, Chroma), Weigert's haematoxylin (Merck), Brilliant Crocein/Acid Fuchsin (Chroma/Merck), 5% phosphotungstic acid (Chroma), and Saffron du Gâtinais (Chroma). After staining, the sections were mounted using Vitro-Clud (Langenbrinck).

For TRAP staining, sections were fixed in 4% PFA, adjusted to pH 5 using sodium acetate and sodium tartrate, and stained using Naphtol AS-MIX-Phosphate and Fast Red Violet LB Salt. A counterstain was carried out with Mayer's Hemalaun solution (Merck). TRAP-positive cells with ≥ 3 nuclei, adherent to the bone surface, were identified as osteoclasts.

Mosaic images were captured using a Leica DM6B microscope with Leica LASX Office software (v.1.4.7). Static and cellular histomorphometry parameters were analyzed using ImageJ, following the guidelines of the American Society for Bone and Mineral Research.

Tissue preparation for MELC

Samples of young mice were prepared as described for histologic analysis. Regions of interest were chosen using consecutive slides of each sample stained with Movat Pentachrome. Cuts were thawed on the day of the MELC experiment. The previously identified regions of interest from up to 6 samples were cut and glued on a cover slide (24 × 60 mm; Menzel-Gläser, Braunschweig, Germany). The fluid chamber holding 100 µl of PBS was created using "press-to-seal" silicone sheets (Life Technologies, Carlsbad, California, USA; 1.0 mm thickness). Permeabilization was performed with 0.2% Triton X-100 in PBS for 10 min at room temperature.

MELC image acquisition

MELC data acquisition of the osteotomy and the healthy control samples was done using either BioDecipher® Device 1.0 (BioDecipher GmbH, Magdeburg, Germany) or a modified Toponome Image Cycler® MM3 (TIC, originally produced by MelTec GmbH & Co.KG, Magdeburg, Germany)[64]. The robot and microscope were controlled using the MelTec TIC-Control software.

Antibodies were titrated in order to find the best working concentration in murine bone marrow tissue, with detailed information provided in Supplementary Table S1 which also contains the staining order and used acquisition parameters for MELC. Prior to each MELC experiment, PBS with 5 % MACS BSA (Miltenyi Biotec, Bergisch Gladbach, Germany) was prepared and used as washing buffer, and Köhler illumination was performed.

Image preprocessing

Images were preprocessed using the TIC OBSERVER software (BioDecipher GmbH, Magdeburg, Germany) and as described in Pascual-Reguant et al. (2021)[65]. Image normalization was performed with ImageJ[66] as previously described in Pascual-Reguant et al. (2021)[65].

Cell segmentation and annotation

Image analysis and cell segmentation were performed using CellProfiler (v.4.2.8). Image intensities were normalized to a scale ranging from 0 to 1. Nuclei were initially identified based on 4′,6-diamidino-2-phenylindole (DAPI) staining, with an expansion step applied to

approximate cell size more accurately. The median fluorescence intensity (MFI) of all markers was quantified within each individual cell and exported as a CSV file for further analysis.

Extracted features were transformed using a hyperbolic arcsine transformation (cofactor = 0.2). Batch correction was implemented using the Harmony algorithm, allowing data integration across different animals and time points. Cell clustering and annotation were performed using DittoSeq[67] (v1.14.3). Marker expression was visualized using UMAP, and annotated clusters were validated by overlaying IF images. Spatial proximity analysis was carried out using SPIAT[68] package (v1.0.0), applying the average_percentage_of_cells_within_radius function to assess spatial proximity of cells to the cortex.

Flow cytometry and cell sorting

Murine bone marrow was flushed out of femorae and tibia of *Tnf* $^{+/+}$ (wild-type) and *Tnf* $^{\Delta ARE/+}$ mice that were generated and kindly provided by George Kollias as previously described [61]. Cells were stained with a mixture of lineage markers (biotinylated CD3e, CD5, CD19, NKp46) marked by streptavidin in BV500, CD45-BV711, Ly6G-FITC, Ly6C-PerCP-eF710, CD163-PE, CD14-PE-Dazzle, NK1.1-PE-Cy7, F4/80-eFluor660, and CD11b-APC-eFluor780. Detailed information for the staining procedure and antibodies is provided in Supplementary Table S2. Dead cells were excluded based on Fixable Viability Dye (FVD-V450) incorporation, and cells of interest were isolated from the CD45 + Ly6G-NK1.1- fraction as CD163^{hi}F4/80^{hi} for tissue resident macrophages and CD14 + F4/80^{lo} for putative *Spp1*^{hi} cells in a Sony MA90 sorter.

Osteoclastogenesis assays

Sorted cells were collected into a-MEM medium with 50 ng/ml M-CSF and plated in 96-well plates in triplicate, each well containing 5000 cells. Cells were left overnight in 50 ng/ml M-CSF and stimulated the following day with 50 ng/ml M-CSF and 100 ng/ml RANKL. Restimulation was performed every two days for six days in total. Cells were subsequently fixed in 4% PFA and stained with the Leukocyte Acid Phosphatase (TRAP) Kit for osteoclast detection as per manufacturer's instructions and imaged in a Keyence Biorevo Microscope.

Statistical analysis

All statistical analysis were performed using R software (v.4.3.3). The choice of parametric and nonparametric tests is indicated in the figure legends, depending on the data distribution and experimental design. *P*-values of less than 0.05 were considered statistically significant. For differential gene expression analysis, genes with adjusted *p*-values of less than 0.001 and an average log-fold change greater than 0.25 were considered significantly expressed. Multiple testing correction was performed using the Benjamini-Hochberg method to control for false discovery rates.

Reporting summary

Further information on research design is available in the Nature Portfolio Reporting Summary linked to this article.

Data availability

Single-cell RNA-seq datasets (raw FASTQ files and processed count matrices) generated in this study are available at the Gene Expression Omnibus under accession number GSE305266. All Seurat objects as well as all MELC data are available in the Zenodo open-access repository (https://zenodo.org/): the Seurat objects are deposited under https://doi.org/10.5281/zenodo.16871641, the MELC images of intact controls can be found under https://doi.org/10.5281/zenodo.16870991, the MELC images of young animals on day 3 under https://doi.org/10.5281/zenodo.16870196, and the MELC images of young animals on day 7 under https://doi.org/10.5281/zenodo.16871121. Finally, the CellProfiler pipeline and its respective output files can be found under https://doi.org/10.5281/zenodo.16876039. All Zenodo records are interlinked within the public repository and can be accessed directly via their respective DOIs. Additionally, Source data are provided with this paper.

References

1. Duda, G. N. et al. The decisive early phase of bone regeneration. *Nat. Rev. Rheumatol.* **19**, 78–95 (2023).
2. Marsell, R. & Einhorn, T. A. Emerging bone healing therapies. *J. Orthop. Trauma* **24**, S4–S8 (2010).
3. Marsell, R. & Einhorn, T. A. The biology of fracture healing. *Injury* **42**, 551–555 (2011).
4. Hernlund, E. et al. Osteoporosis in the European Union: medical management, epidemiology and economic burden. A report prepared in collaboration with the International Osteoporosis Foundation (IOF) and the European Federation of Pharmaceutical Industry Associations (EFPIA). *Arch. Osteoporos.* **8**, 136 (2013).
5. Einhorn, T. A. & Lane, J. M. Significant advances have been made in the way surgeons treat fractures. *Clin. Orthop. Relat. Res.* **355 Suppl**, S2–S3 (1998).
6. Zeckey, C. The aseptic femoral and tibial shaft non-union in healthy patients – an analysis of the health-related quality of life and the socioeconomic outcome. *Open Orthop. J.* **5**, 193–197 (2011).
7. Bucher, C. H. et al. Local immune cell contributions to fracture healing in aged individuals – A novel role for interleukin 22. *Exp. Mol. Med.* **54**, 1262–1276 (2022).
8. Schlundt, C. et al. Individual effector/regulator T cell ratios impact bone regeneration. *Front. Immunol.* **10**, 471374 (2019).
9. Kovtun, A. et al. The crucial role of neutrophil granulocytes in bone fracture healing. *Eur. Cell. Mater.* **32**, 152–162 (2016).
10. Chakravarti, A., Raquil, M.-A., Tessier, P. & Poubelle, P. E. Surface RANKL of Toll-like receptor 4–stimulated human neutrophils activates osteoclastic bone resorption. *Blood* **114**, 1633–1644 (2009).
11. Schlundt, C. et al. Macrophages in bone fracture healing: Their essential role in endochondral ossification. *Bone* **106**, 78–89 (2018).
12. Löffler, J. et al. Compromised Bone Healing in Aged Rats Is Associated With Impaired M2 Macrophage Function. *Front. Immunol.* **10**, 2443 (2019).
13. Bastian, O. W., Koenderman, L., Alblas, J., Leenen, L. P. H. & Blokhuis, T. J. Neutrophils contribute to fracture healing by synthesizing fibronectin+ extracellular matrix rapidly after injury. *Clin. Immunol.* **164**, 78–84 (2016).
14. Soehnlein, O., Lindbom, L. & Weber, C. Mechanisms underlying neutrophil-mediated monocyte recruitment. *Blood* **114**, 4613–4623 (2009).
15. Schlundt, C. et al. The multifaceted roles of macrophages in bone regeneration: A story of polarization, activation and time. *Acta Biomater.* **133**, 46–57 (2021).
16. Hachemi, Y. et al. Multimodal analyses of immune cells during bone repair identify macrophages as a therapeutic target in musculoskeletal trauma. *Bone Res.* **12**, 56 (2024).
17. Perrin, S. et al. Single-nucleus transcriptomics reveal the differentiation trajectories of periosteal skeletal/stem progenitor cells in bone regeneration. *Elife.* **13**, RP92519 (2024).
18. Hoeft, K. et al. Platelet-instructed SPP1+ macrophages drive myofibroblast activation in fibrosis in a CXCL4-dependent manner. *Cell Rep.* **42**, 112131 (2023).
19. Coulis, G. et al. Single-cell and spatial transcriptomics identify a macrophage population associated with skeletal muscle fibrosis. *Sci. Adv.* **9**, eadd9984 (2023).
20. Pappert, M., Khosla, S. & Doolittle, M. Influences of aged bone marrow macrophages on skeletal health and senescence. *Curr. Osteoporos. Rep.* **21**, 771–778 (2023).
21. Yao, Y. et al. The Macrophage-Osteoclast axis in osteoimmunity and osteo-related diseases. *Front. Immunol.* **12**, 664871 (2021).

22. Das, A. et al. Monocyte subsets with high osteoclastogenic potential and their epigenetic regulation orchestrated by IRF8. *J. Bone Miner. Res.* **36**, 199–214 (2020).
23. Tsukasaki, M. et al. Stepwise cell fate decision pathways during osteoclastogenesis at single-cell resolution. *Nat. Metab.* **2**, 1382–1390 (2020).
24. Sun, Y. et al. Macrophage-Osteoclast Associations: Origin, Polarization, and Subgroups. *Front. Immunol.* **12**, 778078 (2021).
25. Takegahara, N., Kim, H. & Choi, Y. Unraveling the intricacies of osteoclast differentiation and maturation: insight into novel therapeutic strategies for bone-destructive diseases. *Exp. Mol. Med.* **56**, 264–272 (2024).
26. Malhan, D., Schmidt-Bleek, K., Duda, G. N. & El Khassawna, T. Landscape of well-coordinated fracture healing in a mouse model using molecular and cellular analysis. *Int. J. Mol. Sci.* **24**, 3569 (2023).
27. Schell, H. et al. Osteoclastic activity begins early and increases over the course of bone healing. *Bone* **38**, 547–554 (2006).
28. Aro, H. T., Wippermann, B. W., Hodgson, S. F. & Chao, E. Y. S. Internal remodeling of periosteal new bone during fracture healing. *J. Orthop. Res.* **8**, 238–246 (1990).
29. Chung, P. L. et al. Effect of Age on Regulation of Human Osteoclast Differentiation. *J. Cell. Biochem.* **115**, 1412 (2014).
30. Bucher, C. H. et al. Experience in the adaptive immunity impacts bone homeostasis, remodeling, and healing. *Front. Immunol.* **1**, 797. www.frontiersin.org. (2019).
31. Baccin, C. et al. Combined single-cell and spatial transcriptomics reveal the molecular, cellular and spatial bone marrow niche organization. *Nat. Cell Biol.* **22**, 38–48 (2020).
32. Zheng, X. et al. Short-read and long-read RNA sequencing of mouse hematopoietic stem cells at bulk and single-cell levels. *Sci. Data 2021* **8**, 1–10 (2021).
33. Xie, X. et al. Single-cell transcriptome profiling reveals neutrophil heterogeneity in homeostasis and infection. *Nat. Immunol.* **21**, 1119–1133 (2020).
34. Grieshaber-Bouyer, R. et al. The neutrotime transcriptional signature defines a single continuum of neutrophils across biological compartments. *Nat. Commun.* **12**, 2856 (2021).
35. Hansen, M. S. et al. Transcriptional reprogramming during human osteoclast differentiation identifies regulators of osteoclast activity. *Bone Res.* **12**, 5 (2024).
36. Biniaris-Georgallis, S.-I. et al. Amplification of autoimmune organ damage by NKp46-activated ILC1s. *Nature* **634**, 952–960 (2024).
37. Morse, C. et al. Proliferating SPP1/MERTK-expressing macrophages in idiopathic pulmonary fibrosis. *Eur. Respir. J.* **54**, 1802441 (2019).
38. Corcoran, J. A. & Napier, B. A. C3aR plays both sides in regulating resistance to bacterial infections. *PLoS Pathog.* **18**, e1010657 (2022).
39. Ebong, S. J. et al. Critical Role of CD14 for Production of Proinflammatory Cytokines and Cytokine Inhibitors during Sepsis with Failure To Alter Morbidity or Mortality. *Infect. Immun.* **69**, 2099–2106 (2001).
40. Yi, Z., Liu, Y., Wang, J., Hu, C. & Man, Y. Spp1 secreted by macrophages impairs osteogenic ability of Ctsk$^+$Fmod$^+$periosteal cells in jaw bone. Preprint at https://doi.org/10.1101/2023.05.23.541910 (2023).
41. Shu, L. Z., Zhang, X. L., Ding, Y. D. & Lin, H. From inflammation to bone formation: the intricate role of neutrophils in skeletal muscle injury and traumatic heterotopic ossification. *Exp. Mol. Med.* **56**, 1523–1530 (2024).
42. Sawant, K. V. et al. Neutrophil recruitment by chemokines Cxcl1/KC and Cxcl2/MIP2: Role of Cxcr2 activation and glycosaminoglycan interactions. *J. Leukoc. Biol.* **109**, 777–791 (2021).
43. Li, G. et al. PPARG/SPP1/CD44 signaling pathway in alveolar macrophages: Mechanisms of lipid dysregulation and therapeutic targets in idiopathic pulmonary fibrosis. *Heliyon* **11**, e41628 (2025).
44. Lee, D. et al. CCL4 enhances preosteoclast migration and its receptor CCR5 downregulation by RANKL promotes osteoclastogenesis article. *Cell Death Dis.* **9**, 1–12 (2018).
45. Yamashiro, Y. et al. Matrix mechanotransduction mediated by thrombospondin-1/integrin/YAP in the vascular remodeling. *Proc. Natl. Acad. Sci. USA.* **117**, 9896–9905 (2020).
46. Amend, S. R. et al. Thrombospondin-1 regulates bone homeostasis through effects on bone matrix integrity and nitric oxide signaling in osteoclasts. *J. Bone Miner. Res.* **30**, 106 (2015).
47. Kaur, S. & Roberts, D. D. Emerging functions of thrombospondin-1 in immunity. *Semin. Cell Dev. Biol.* **155**, 22–31 (2024).
48. Capobianco, C. A., Hankenson, K. D. & Knights, A. J. Temporal dynamics of immune-stromal cell interactions in fracture healing. *Front. Immunol.* **15**, 1352819 (2024).
49. Johannesdottir, F. et al. Age-related changes in bone density, microarchitecture, and strength in postmenopausal black and white women: the SWAN longitudinal HR-pQCT study. *J. Bone Miner. Res.* **37**, 41–51 (2022).
50. Mi, B. et al. Ageing-related bone and immunity changes: insights into the complex interplay between the skeleton and the immune system. *Bone Res.* **12**, 1–15 (2024).
51. Ruiz-Rosado, J. D. et al. Neutrophil-macrophage imbalance drives the development of renal scarring during experimental pyelonephritis. *J. Am. Soc. Nephrol.* **32**, 69–85 (2021).
52. Hunninghake, G. W. et al. Characterization of the inflammatory and immune effector cells in the lung parenchyma of patients with interstitial lung disease. *Am. Rev. Respir. Dis.* **123**, 407–412 (1981).
53. He, W. et al. Neutrophil heterogeneity and plasticity: unveiling the multifaceted roles in health and disease. *MedComm.* **6**, e70063 (2025).
54. Zhang, J. et al. Dysregulation of neutrophil in sepsis: recent insights and advances. *Cell Commun. Signal.* **23**, 1–17 (2025).
55. Maeda, K. et al. Wnt5a-Ror2 signaling between osteoblast-lineage cells and osteoclast precursors enhances osteoclastogenesis. *Nat. Med.* **18**, 405–412 (2012).
56. Uehara, S. et al. Protein kinase N3 promotes bone resorption by osteoclasts in response to Wnt5a-Ror2 signaling. *Sci. Signal.* **10**, eaan0023 (2017).
57. Chen, K. et al. Sfrp4 repression of the Ror2/Jnk cascade in osteoclasts protects cortical bone from excessive endosteal resorption. *Proc. Natl. Acad. Sci. USA.* **116**, 14138–14143 (2019).
58. Kong, Y. Y. et al. OPGL is a key regulator of osteoclastogenesis, lymphocyte development and lymph-node organogenesis. *Nature* **397**, 315–323 (1999).
59. Lam, J. et al. TNF-α induces osteoclastogenesis by direct stimulation of macrophages exposed to permissive levels of RANK ligand. *J. Clin. Investig.* **106**, 1481–1488 (2000).
60. Ambrosi, T. H. et al. Adipocyte accumulation in the bone marrow during obesity and aging impairs stem cell-based hematopoietic and bone regeneration. *Cell Stem Cell* **20**, 771 (2017).
61. Kontoyiannis, D., Pasparakis, M., Pizarro, T. T., Cominelli, F. & Kollias, G. Impaired on/off regulation of TNF biosynthesis in mice lacking TNF AU- rich elements: Implications for joint and gut-associated immunopathologies. *Immunity* **10**, 387–398 (1999).
62. Butler, A., Hoffman, P., Smibert, P., Papalexi, E. & Satija, R. Integrating single-cell transcriptomic data across different conditions, technologies, and species. *Nat. Biotechnol. 2018* **36**, 411–420 (2018).
63. Korsunsky, I. et al. Fast, sensitive and accurate integration of single-cell data with Harmony. *Nat. Methods* **16**, 1289–1296 (2019).
64. Holzwarth, K. et al. Multiplexed fluorescence microscopy reveals heterogeneity among stromal cells in mouse bone marrow sections. *Cytom. A* **93**, 876–888 (2018).
65. Pascual-Reguant, A. et al. Multiplexed histology analyses for the phenotypic and spatial characterization of human innate lymphoid cells. *Nat. Commun.* **12**, 1–15 (2021).

66. Abramoff, M. D., Magalhaes, P. J. & Ram, S. J. Image Processing with ImageJ. *Biophotonics Int.* **11**, 36–42 (2004).
67. Bunis, D. G., Andrews, J., Fragiadakis, G. K., Burt, T. D. & Sirota, M. dittoSeq: universal user-friendly single-cell and bulk RNA sequencing visualization toolkit. *Bioinformatics* **36**, 5535–5536 (2021).
68. Feng, Y. et al. Spatial analysis with SPIAT and spaSim to characterize and simulate tissue microenvironments. *Nat. Commun.* **14**, 1–20 (2023).

Acknowledgements

We are grateful for the excellent technical assistance of Gabriela Korus, Mario Thiele and Katrin Vogt. We also thank the BIH/MDC Genomics Technology Platform and the Core Unit Bioinformatics for their support and expertise in single-cell sequencing and data analysis.

Author contributions

A.N. has participated in the conception and design of the study, acquisition and analysis of all data, and manuscript writing. H.Z.O. contributed to single-cell study design and data acquisition. D.M.M. participated in the analysis of all data and manuscript writing. S.K. contributed to the design of the MELC experiments and was involved in MELC data acquisition and analysis. A.K., assisted by P.B., performed flow cytometry, cell sorting, ex vivo osteoclastogenesis assays, and the corresponding data analysis. A.E., M.K. and K.S.B. contributed to the design and coordination of the animal studies. O.B. has participated in the analysis of single-cell data. R.U. and R.G. conducted the MELC experiments. C.H.B., A.H., S.H. and KSB provided conceptual input and contributed to discussions throughout the project. A.T., A.E.H., B.S., G.N.D. contributed to the conception and design of the study. All authors contributed to data interpretation and manuscript editing, and approved the final version of the manuscript.

Funding

This work was supported by the German Research Foundation (DFG), through Collaborative Research Centre CRC 1444 (project P11 to AT, project P13 to BS and GND, and project P14 to AEH). GND further acknowledges support from the European Research Council (ERC) Advanced Grant "Immuno-Mechanics". Open Access funding enabled and organized by Projekt DEAL.

Competing interests

The authors declare no competing interests.

Additional information

Supplementary information The online version contains supplementary material available at https://doi.org/10.1038/s41467-026-77196-7.

Correspondence and requests for materials should be addressed to Georg N. Duda.

Peer review information *Nature Communications* thanks the anonymous reviewers for their contribution to the peer review of this work. A peer review file is available.

Anne Noom[1,2,3], Hülya Zeynep Oktay[4,5,14], Duncan M. Morgan[1,3,6,14], Sandy Kroh[7,8,14], Ana Kasapi[7,9,10,14], Agnes Ellinghaus[1,2,3], Merle Kochan[1,2,3], Olufemi Bolaji[4,5], Ralf Uecker[7,8], Robert Günther[7,8], M. Paula Bianchi[7,9,10], Christian H. Bucher[1,2], Alexander Hildebrandt[3], Simon Haas[11,12,13], Katharina Schmidt-Bleek[1,2,3], Antigoni Triantafyllopoulou[7,9,10], Anja E. Hauser[7,8], Birgit Sawitzki[4,5] & Georg N. Duda[1,2,3,6] ✉

[1]Julius Wolff Institute (JWI), Berlin Institute of Health at Charité – Universitätsmedizin Berlin, Berlin, Germany. [2]BIH Center for Regenerative Therapies (BCRT), Berlin Institute of Health at Charité – Universitätsmedizin Berlin, Berlin, Germany. [3]Center for Musculoskeletal Surgery, Charité – Universitätsmedizin Berlin, Berlin, Germany. [4]Department of Infectious Diseases and Respiratory Medicine, Charité – Universitätsmedizin Berlin, Corporate Member of Freie Universität Berlin and Humboldt University of Berlin, Berlin, Germany. [5]Center of Immunomics, Berlin Institute of Health at Charité – Universitätsmedizin Berlin, Berlin, Germany. [6]Wyss Institute for Biologically Inspired Engineering and John A. Paulson School of Engineering and Applied Sciences, Harvard University, Cambridge, MA, USA. [7]Department of Rheumatology and Clinical Immunology, Charité-Universitätsmedizin Berlin Corporate Member of Freie Universität Berlin and Humboldt-Universität zu Berlin, Berlin, Germany. [8]Immune Dynamics, Deutsches Rheuma-Forschungszentrum (DRFZ), a Leibniz Institute, Berlin, Germany. [9]Institute of Microbiology, Infectious Diseases and Immunology (I-MIDI), Charité-Universitätsmedizin Berlin Campus Benjamin Franklin, Berlin, Germany. [10]Deutsches Rheuma-Forschungszentrum (DRFZ), a Leibniz Institute, Berlin, Germany. [11]Berlin Institute of Health at Charité, Universitätsmedizin Berlin, Berlin, Germany. [12]Berlin Institute of Medical Systems Biology, Max Delbrück Center for Molecular Medicine in the Helmholtz Association, Berlin, Germany. [13]Precision Healthcare University Research Institute, Queen Mary University of London, London, UK. [14]These authors contributed equally: Hülya Zeynep Oktay, Duncan M. Morgan, Sandy Kroh, Ana Kasapi. ✉e-mail: georg.duda@charite.de